Numerical investigation of cavitation erosion in high-pressure fuel injector in the presence of surface deviations

Fuel 386 (2025) 134174

Contents lists available at ScienceDirect

Fuel

journal homepage: www.elsevier.com/locate/fuel

Full length article

Numerical investigation of cavitation erosion in high-pressure fuel injector in the presence of surface deviations

Mehmet Özgünoğlu [a,*], Gerard Mouokue [c], Michael Oevermann [a,b], Rickard E. Bensow [a]

[a] Chalmers University of Technology, Gothenburg, Sweden
[b] Brandenburgische Technische Universität Cottbus-Senftenberg (BTU), Cottbus, Germany
[c] Woodward L'Orange GmbH, Stuttgart, Germany

ARTICLE INFO

Keywords:
Fuel injector
CFD
Cavitation erosion
Surface deviations

ABSTRACT

This study investigates cavitation-induced erosion in high-pressure fuel injectors using numerical simulations, focusing on the effects of surface deviations, turbulence modeling, and a refined approach for the erosion assessment. The proposed erosion model combines advanced erosion indicators to enhance predictive accuracy while addressing limitations in existing methodologies. Cavitation dynamics are simulated with the modified Zwart–Gerber–Belamri model, employing Reynolds-averaged Navier–Stokes (RANS) and Large Eddy Simulation (LES) approaches. Numerical results for a high-lift needle position are validated against experimental data, providing insights into erosion behavior in industrial heavy-duty injectors. Both Computer-Aided Design (CAD) and Tomography Scan (TS) models are used to evaluate the impact of surface deviations on erosion patterns. Results reveal that incorporating surface deviations reduces the vapor volume and alters the erosion patterns. LES simulations exhibit enhanced sensitivity to the surface deviations, capturing finer turbulence structures and local pressure fluctuations, whereas RANS provides reasonable accuracy with lower computational cost.

1. Introduction

The environmental impact of heavy-duty engines, especially in maritime applications, is crucial. Shifting to sustainable solutions is essential for reducing emissions. Dual-fuel engines, which can use both liquid fuel and a cleaner alternative such as natural gas, are becoming increasingly important in this sector. Their ability to switch between fuels offers operational flexibility and is a significant step towards greener maritime practices, demonstrating a commitment to reducing the environmental footprint in shipping.

The existence of high-pressure within the injector is a necessary industrial requirement since it is needed to provide efficient mixing/combustion processes while taking into consideration stringent emission regulations [1]. Here, high-pressure fuel injectors, in particular heavy-duty dual-fuel engines, are pivotal for delivering the liquid pilot fuel efficiently into the combustion chamber, playing an important role in initiating and controlling the combustion process. The precision and timing of these injectors directly influence engine performance, fuel efficiency, and emission characteristics. The development and optimization of these injectors are essential, with advancements focusing on better fuel delivery control. This is particularly important in dual fuel engines, where balancing the injection of liquid and gaseous fuel is key for optimal performance.

High pressure environment and geometrical considerations cause sudden local velocity changes within the fuel injector. As a result of these sudden changes in velocity, the injector is more likely prone to cavitation, which occurs if the local pressure becomes less than the vapor pressure.

In fuel injectors, there are two forms of cavitation that can occur. The first, known as geometric cavitation, is caused by direct interaction of the geometry (walls) with the flow (bending of streamlines). It typically appears as a film-like sheet cavity formation within the nozzle. This mainly originates at the entrance of the orifice hole due to the local pressure drop induced by the orifice inlet hole geometry [2]. This type of cavitation is more pronounced in high lift needle position. The second type is referred to as string cavitation, which is due to the low pressure regions created by the filament-like vortical structures. While it is understood that both varieties of cavitation influence the characteristics of the fuel spray, the specific impacts of geometrical

* Corresponding author.
E-mail address: omehmet@chalmers.se (M. Özgünoğlu).

https://doi.org/10.1016/j.fuel.2024.134174
Received 20 September 2024; Received in revised form 30 November 2024; Accepted 20 December 2024
Available online 8 January 2025

cavitation and string cavitation have not been distinctly defined [3].

In fuel injectors, the occurrence of these cavitation structures is not just a matter of internal fluid dynamics but also significantly impacts the injector's structural integrity. The presence of these cavitation types leads to variation in fuel flow and spray patterns, which are critical for efficient engine combustion.

Transitioning from general cavitation impacts, a key concern is cavitation erosion. This process, in which cavitation structures collapsing near the injector surfaces, results in material erosion. This erosion compromises injector durability and performance, impacting both the fuel mixing and combustion processes.

So, this wear mechanism not only reduces the efficiency of the injector over time but also raises concerns about the longevity and maintenance of the fuel injection system. Moreover, material loss due to surface erosion makes the fuel injection system vulnerable to catastrophic system failures.

Conducting experiments on cavitation erosion for high pressure fuel injection systems presents challenges due to the need for specialized equipment capable of replicating extreme pressure conditions accurately while maintaining precise control over fluid dynamics and cavitation phenomena. On the other hand, the ongoing technological development in computational power makes computational techniques a desired tool in the design phase of fuel injection systems. However, cavitation erosion assessment via numerical approaches for industrial high-pressure fuel injectors is still challenging as it requires computationally expensive simulations of flows with a wide range of time and length scales [4]. In addition, a significant challenge lies in the lack of universally valid cavitation models, further complicating the accurate prediction of erosion.

Numerical assessment of cavitation erosion, conducted by various research groups, have explored a wide range of contexts beyond fuel injectors. These studies take into account diverse physical mechanisms and employ high-fidelity methods to understand cavitation erosion in different environments, such as in propellers, hydrofoils, and other hydraulic components. The numerical methods employed in these studies demonstrate variability in how they address compressibility effects, turbulence modeling, and multiphase flow modeling.

Dular et al. [5] introduced a model based on the detailed physical mechanism of cavitation erosion. These include the implosion of cavitation clouds, the pressure waves, the creation of micro-jets, and the formation of pits [6]. Bensow and Bark [7] employed LES to study cavitating flows over a propeller. Their findings, which align with experimental observations, suggest that LES can effectively capture crucial cavitation mechanisms such as reentrant jets and sheet cavity dynamics, which are important to correctly detect erosion [7].

Li et al. [8] proposed an erosion intensity function to assess the risks of cavitation erosion on hydrofoil surfaces. This function, derived from unsteady RANS simulations, is based on the average of the time derivative of the local pressure above a certain threshold.

Mihatsch et al. [9] used a density-based finite volume method. This method considers the compressibility of both fluid phases and captures the pressure waves induced by collapses. The study focuses on detecting and quantifying vapor structure collapses within the fluid domain, using the expansion of a liquid into a radially divergent gap as a reference. This setup exhibits unsteady sheet and cloud cavitation characteristics.

Peters et al. [10] presented an erosion model that relies on the micro-jet hypothesis. This model uses flow solution data to pinpoint areas prone to micro-jet occurrence. The model's effectiveness in simulating cavitating flows was validated through experimental comparisons involving sheet cavitation on a NACA 0009 hydrofoil. Furthermore, their multi-scale Euler–Lagrange method effectively evaluates cavitation-induced erosion, aligning with observed erosion pit sizes and potentials [11].

Schenke [12] introduced a novel method for assessing the erosive aggressiveness of cavitating flows through numerical simulations. This technique utilizes the cavitation intensity approach combined with impact power functions to predict the impact power of cavity collapses. A method based on the concept of energy cascading in cavitation erosion developed by Arabnejad et al. [13,14] has been effectively used to evaluate the risk of cavitation erosion in an incompressible formulation. This method takes into account both micro-jets and shock waves as key factors in cavitation erosion.

The above studies show that numerical assessment of cavitation erosion have been investigated and tested by many research groups. Experimental facilities are utilized to test and validate the accuracy of the developed models.

In the context of the fuel injector, the experimental techniques are more applicable for low-pressure systems targeting prevention and detection of cavitation-induced erosion inside the fuel injector. The difficulty in performing experiments in a laboratory environment is a known fact due to the nature of high-pressure operating conditions. Moreover, computational investigation is practical if one would like to see the effects of the geometrical alterations in the design phase of the high-pressure injector, which is the main factor for the cavitation-induced erosion. Hence, a numerical investigation of cavitation-induced erosion is a desirable tool.

Numerical assessment of cavitation-induced erosion in fuel injectors can be grouped into the following categories: modeling with density-based and pressure-based solvers, taking into account different turbulence and cavitation closures, and assessment of cavitation-induced erosion with different erosion indicator metrics.

Örley et al. [15] performed well-resolved LES methodology inside a nine-hole common rail diesel injector during a full injection cycle using a fully compressible flow solver. They have also configured different simulations for steady needle lift conditions. Their conclusion is that consideration of the unsteady needle motion is necessary for accurate prediction of erosion sensitive areas.

An explicit density-based approach is applied with real-fluid thermodynamic closure by Kolovos et al. [16]. They used different types of thermodynamic closures with the WALE–LES model and investigated the fuel heating and cavitation erosion location relationship during the needle movement for the five-hole injector. They were in good agreement with their numerical results against the X-ray derived surface erosion images. Another compressible simulation was done by Falsafi et al. [17]. They used real geometries and considered the entire injection cycle with time-dependent rail pressure and transient needle movement.

Santos et al. [18] applied LES methodology with the moving mesh technique using ANSYS to investigate cavitation erosion of a gasoline direct injection (GDi) type injector. Having erosion damage images from the injector durability test, they investigated various erosion indicators and concluded that the accumulated erosive power is the most promising indicator for predicting cavitation erosion. Another LES simulation of a diesel injector is presented in Koukouvinis et al. [19]. They simulated two similar injector designs together with the X-ray CT scans. The pressure peak due to vapor collapse is determined as a main tool to assess the cavitation erosion. The predicted pressure peak locations showed particularly good agreement with the observed erosion patterns.

Koukouvinis et al. [20] numerically investigated the high-pressure fuel pump as well. Here, they used a barotropic equation of state with a homogeneous equilibrium model. The locations susceptible to cavitation-induced erosion are identified based on the concept of an adverse pressure gradient, which serves as the necessary cause for the collapse of cavitation structures.

Brunhart [21] studied the predictive capability of different erosion indicators for two fuel injection systems. His motivation was to compare the original eroding design with a modified non-eroding design together with the experimental erosion images. In this benchmark study, DES and RANS turbulence modeling approaches are investigated.

Squared material derivative, $(DP/Dt)^2$, and second derivative of potential power density, $PPD2$ [22], were the most promising erosion indicators among the ones investigated.

Cristofaro et al. [23] simulated the generic Spray A case from the Engine Combustion Network (ECN) with the implicit compressible pressure-based and three-phase algorithm. They used the Coherent Structure Model as an LES model for subgrid turbulence. Cavitation erosion prone locations are evaluated by recording the maximum intensity of pressure on the surface. Later, they applied the same algorithm to simulate cavitation in a diesel injector [24]. Here, they particularly investigated the effect of the geometry alterations caused by cavitation erosion by analyzing the nominal design geometry and the eroded one. One of the purposes of their study was to assess cavitation erosion. The conclusion was that the recorded pressure peaks on the nominal geometry fit well with the eroded regions of the experiments. Moreover, they applied the same cavitation erosion assessment strategy [25] to the well-reported micro throttle [26].

Zang et al. [27] conducted simulations to investigate the effects of nozzle K-factor, defined as the ratio of the inlet–outlet diameter difference to the nozzle length, and needle lifts on the cavitating flow field and erosion risk within a diesel nozzle featuring a double array of holes. The relative risk of surface erosion served as an index for evaluating cavitation erosion risk on nozzle hole surfaces. The results showed that increasing the K-factor significantly reduced cavitation intensity on hole surfaces, causing cavitation to retract towards the orifice entrance.

Kumar's study [28] evaluates the Zwart–Gerber–Belamri (ZGB) cavitation model coupled with the RANS turbulence model and taking into account the compressibility of both gas and liquid phases. Here, the quantitative and qualitative comparison has been done against experimental data and flow field analysis reveals the formation of vortices in the injector sac volume, including "hole-to-hole" connecting vortices and double "counter-rotating" vortices from the needle wall.

Wang et al. [29] investigate the internal flow characteristics and spray patterns of double-layer multi-hole diesel engine injector nozzles. Both experimental and computational approaches were employed to analyze variations between upper and lower layer nozzle holes. Actual geometry derived from X-ray scans facilitated accurate characterization of individual injection holes. Results indicated more intense cavitation development in upper layer holes, leading to higher injection rates and less cycle-to-cycle variations in spray patterns from lower layer holes.

Magnotti's work [30] introduced the Cavitation-Induced Erosion Risk Assessment (CIERA) tool, which connects multiphase flow simulation predictions with material erosion progression. The tool's development involved validating cavitation and erosion predictions for pressurized diesel fuel flow within channel geometries, including variations in Reynolds and cavitation numbers and different inlet corner geometries. The multiphase flow within the channel was modeled using a compressible mixture model with a homogeneous relaxation model for phase change and a dynamic structure approach with LES for turbulent flow. CIERA predictions demonstrated accurate qualitative and quantitative assessment performances when the results are compared with the experiments.

Mariasiu et al. [31] analyze the impact of different biofuels on erosion during the injection process. The research highlights varying levels of erosion intensity in injector nozzles when using diesel fuel compared to biodiesel and pure vegetable oil. Their findings emphasize the importance of enhancing injection system design and maintenance practices for compression ignition engines fueled with biodiesel.

Mouvanal et al. [32] followed a numerical procedure and aimed at predicting potential erosion caused by cavitation in flow devices such as throttles and nozzles. The proposed technique efficiently captures periodic vapor cloud shedding and collapse, allowing for the prediction of cavitation erosion zones. An algorithm detects collapse pressures indicative of material erosion due to cavitation. Numerical predictions were validated against experimental data, suggesting potential application in reducing the design cycle time of fuel injectors.

Previous studies have explored a variety of erosion metrics, turbulence models, multiphase models, and flow conditions, highlighting the key physical mechanisms such as cavitation cloud implosions and the generation of high-pressure micro-jets. These efforts have provided valuable insights into the detection of erosion-sensitive areas in high-pressure fuel injectors. However, a major limitation of many studies lies in the use of idealized geometries, which fail to capture the manufacturing deviations present in real-world applications. Realistic geometry modeling plays a pivotal role in accurately simulating cavitation dynamics and erosion patterns. Manufacturing deviations, often overlooked in Computer-Aided Design (CAD) models, can significantly influence cavitation behavior, especially in high-pressure environment.

Although surface deviations (e.g., due to manufacturing processes) and surface irregularities (e.g., roughness and scratches) are often discussed together, they are not identical. Surface deviations refer to manufacturing-induced geometrical variations, while surface irregularities typically encompass smaller-scale roughness and scratches. For example, Lin et al. [33] demonstrated that higher initial surface roughness leads to increased mass loss, as rough surfaces act as initiation sites for cavitation bubble formation and collapse. Similarly, Lu et al. [34] found that scratches on the surface could enhance cavitation erosion resistance, particularly in the early stages of erosion. Interestingly, scratches had a greater effect on the cavitation erosion resistance of coatings than on substrates. Despite these insights, prior studies have largely neglected the broader impact of manufacturing deviations on cavitation and erosion behavior, a critical gap addressed in this study.

Despite these findings, there are, to the best of the authors' knowledge, no studies that directly investigate the specific effects of surface or manufacturing deviations on cavitation and cavitation erosion. This gap is critical because such deviations introduce complex flow interactions that may significantly alter erosion predictions, particularly in high-pressure fuel injector systems. Addressing this gap is essential for advancing cavitation modeling and improving the predictive accuracy of erosion assessments in real-world applications.

In addition to geometry considerations, the choice of numerical methodology significantly impacts the predictive accuracy of cavitation modeling. Reynolds-Averaged Navier–Stokes (RANS) and Large Eddy Simulation (LES) are widely used approaches, each offering distinct advantages. LES captures detailed turbulence structures and provides insights into complex flow phenomena, but its high computational cost often limits its use in industrial applications. RANS, on the other hand, offers a more computationally efficient alternative, though it may lack the fidelity needed to resolve intricate cavitation dynamics.

This study uniquely discusses the RANS vs. LES trade-off by evaluating both methodologies under the influence of surface deviations. Furthermore, it proposes a unified approach for cavitation erosion assessment. The erosion model relies on preventing fake collapses, as emphasized in [32], and utilizes the promising erosion indicators presented in [21]. Hence, this methodology addresses existing gaps and enhances the prediction accuracy of cavitation-induced erosion by integrating two complementary techniques. By coupling this unified framework with an analysis of realistic surface deviations and the RANS vs. LES trade-off, the study provides a more comprehensive and robust perspective on erosion behavior under complex flow conditions.

In this study, both RANS and LES turbulence modeling approaches are evaluated with corresponding $k-\omega$ SST [35] and WALE [36] submodels. For RANS, the turbulent viscosity is redefined with Reboud's correction [37]. Assuming a homogeneous mixture, cavitation is modeled via a transport equation approach with mass transfer modeling. Therefore, the Zwart–Gerber–Belamri cavitation model [38] is used with altered model coefficients, as will be elaborated below.

The numerical results have been thoroughly compared with the experimental data, providing valuable insights into cavitation erosion behavior. The impact of surface deviations on erosion patterns has

been examined, contributing to a better understanding of cavitation-induced erosion. Consequently, this study emphasizes the importance of coupling computational models with industrial practice, moving beyond simplified academic cases to address the complex interplay of factors encountered in real-world applications.

This work contributes to bridging the gap between academic research and industrial practice by following objectives:

- Investigate the influence of surface deviations on cavitation dynamics and erosion patterns in high-pressure injectors.
- Evaluate the trade-off between RANS and LES methodologies for erosion prediction under the effect of realistic surface deviations.
- Propose and validate a unified erosion modeling framework to address existing limitations.

2. Methodology

2.1. Multi-phase modeling

Assuming a homogeneous mixture, multi-phase flow is modeled here with the so called "Mixture model". Liquid and vapor phases behave as they are in local equilibrium over short spatial length scales [39].

The continuity equation for the mixture is given by,

$$\frac{\partial}{\partial t}\left(\rho_m\right) + \nabla \cdot \left(\rho_m \overrightarrow{V_m}\right) = 0, \tag{1}$$

where V_m and ρ_m are the mass averaged velocity and mixture density, respectively, which are given in detail below. Here, α_k is the volume fraction of phase k, ρ_k is the density of phase k, and $\overrightarrow{V_k}$ is the velocity of phase k,

$$\overrightarrow{V_m} = \frac{\sum_{k=1}^{n} \alpha_k \rho_k \overrightarrow{V_k}}{\rho_m}, \tag{2}$$

$$\rho_m = \sum_{k=1}^{n} \alpha_k \rho_k. \tag{3}$$

Summation of the individual momentum equation for all phases can represent the momentum equation for the mixture. In the form given, the effect of gravity and body force are neglected,

$$\frac{\partial}{\partial t}\left(\rho_m \overrightarrow{V_m}\right) + \nabla \cdot \left(\rho_m \overrightarrow{V_m}\overrightarrow{V_m}\right) = -\nabla p + \nabla \cdot \left[\mu_m \left(\nabla \overrightarrow{V_m} + \nabla \overrightarrow{V_m^T}\right)\right] \tag{4}$$

Here, μ_m is the viscosity of the mixture given by

$$\mu_m = \sum_{k=1}^{n} \alpha_k \rho_k \ . \tag{5}$$

Although there are elevated temperature rises during a cavitation collapse event, time and length scale of these instances are limited, and they have a negligible effect on the global fluid properties [40]. Therefore, the effect of temperature is not taken into consideration and the energy equation is not being solved.

2.2. Cavitation modeling

The vapor transport equation relates mass transfer between the liquid and vapor phases with the equation

$$\frac{\partial}{\partial t}\left(\alpha\ \rho_v\right) + \nabla \cdot \left(\alpha\ \rho_v\ \overrightarrow{V_v}\right) = R_e - R_c. \tag{6}$$

Here, ρ_v is vapor density, α is vapor volume fraction, and $\overrightarrow{V_v}$ represents vapor phase velocity field. R_e and R_c are the mass transfer source terms, which represent evaporation and condensation, respectively.

The Zwart–Gerber–Belamri (ZGB) model is selected to model mass transfer. The ZGB model uses the following rates of mass transfers, first described by Zwart et al. [38]:

$$P \le P_v: \qquad R_e = F_v \frac{3\alpha_{nuc}\left(1-\alpha_v\right)\rho_v}{R_b}\sqrt{\frac{2}{3}\frac{P_v - P}{\rho_l}}, \quad R_c = 0, \tag{7}$$

Table 1
ZGB Mass transfer coefficients.

Description of the coefficient	Numerical value
R_b: Bubble radius [m]	1×10^{-6}
α_{nuc}: Nucleation site volume fraction	5×10^{-4}
F_v: Evaporation coefficient	500
F_c: Condensation coefficient	0.1
P_v: Vaporization pressure [Pa]	6000

$$P \ge P_v: \qquad R_c = F_c \frac{3\alpha_{nuc}\ \alpha_v\ \rho_v}{R_b}\sqrt{\frac{2}{3}\frac{P - P_v}{\rho_l}}, \quad R_e = 0. \tag{8}$$

The mass transfer rate constants are provided in Table 1. To assess the influence of ZGB parameters on cavitation dynamics, a sensitivity analysis was conducted by systematically varying the evaporation (F_v) and condensation (F_c) coefficients. The goal of this study was to evaluate how these coefficients influence key aspects of cavitation behavior, such as the spatial distribution of collapse pressures and the extent of cavitation-induced erosion. Specifically, both coefficients were increased to 10 times their default values, and the resulting impact on the phase-change dynamics was examined.

An important aspect considered in this study was the occurrence of minimum pressure values in the flow field. Previous studies [21,41] highlighted that negative pressures can arise as a numerical artifact due to insufficient mass transfer rates in cavitation models. Such unrealistic negative pressures can compromise the physical accuracy of the simulation results and hinder meaningful comparisons with experimental data.

The sensitivity analysis revealed that increasing the ZGB coefficients enhances the mass transfer rate, aligning the model more closely with thermodynamic equilibrium conditions. Furthermore, this led to an enhanced correlation between the numerical erosion result and the experimental results.

These findings informed the selection of the optimal ZGB parameters used in this study, ensuring a balance between numerical stability and predictive accuracy. The calibrated parameters were applied to both RANS and LES simulations to achieve consistent results across different modeling approaches.

For this purpose, both coefficients were increased to ten times their default values.

2.3. Thermodynamic modeling

Diesel is modeled as a compressible liquid and represented with the Tait equation of state. The barotropic formulation enables to model the liquid phase without nonphysical pressure spikes under high-pressure conditions. It is represented in the simplified form with the following set of equations [39]:

$$\left(\frac{\rho}{\rho_0}\right)^n = \frac{K}{K_0}, \tag{9}$$

$$K = K_0 + n\Delta p, \tag{10}$$

$$\Delta p = p - p_0. \tag{11}$$

Relevant description of the parameters and values are given in Table 2. Diesel vapor is modeled as an incompressible fluid with physical properties given in Table 3 below. Although the vapor phase is incompressible, the mixture can still be considered as compressible [41].

2.4. Turbulence modeling

2.4.1. RANS $k-\omega$ SST model

The shear-stress transport $k-\omega$ turbulence model ($k-\omega$ SST) [35] is employed within the unsteady (RANS) formulation. It effectively blends the $k-\omega$ and $k-\epsilon$ models in the regions of near-wall and free-stream, respectively. Hence, robustness and accuracy are provided with the

Table 2
Diesel liquid properties.

Description	Value
p_0 = reference pressure [Pa]	0
ρ_0 = reference density [kg/m^3]	771.13
K_0 = reference bulk modulus [Pa]	8.179023×10^8
n = density exponent	7.15

Table 3
Diesel vapor properties.

Description	Value
Density [kg/m^3]	0.89457
Viscosity [kg/(ms)]	8×10^{-6}

help of blending functions [39].

A special treatment is applied to the turbulent viscosity, μ_t, which was previously proposed by Reboud et al. [37]. It is an *ad hoc* method to reduce eddy viscosity in the mixture to allow for a more dynamic flow behavior. The correction is expressed as

$$\mu_t = \frac{\rho' k}{\omega} \frac{1}{\max\left[\frac{1}{\alpha^*}, \frac{S\ F_2}{a_1 \omega}\right]}, \tag{12}$$

$$\rho' = \rho_v + \frac{\left(\rho_m - \rho_v\right)^n}{\left(\rho_l - \rho_v\right)^{n-1}}, \tag{13}$$

$$\rho_m = \alpha \rho_v + (1-\alpha)\rho_l. \tag{14}$$

Here, the proposed density function ρ' returns a value in the mixture, including the corresponding phase contributions. In this way, unrealistically high values of the turbulent viscosity are prevented and an unsteadiness of cavitation is achieved [42]. This correction is applied via User Defined Function (UDF) implementation.

2.4.2. LES Wale model

In the Wall-Adapting Local Eddy-Viscosity (WALE) model [36] the turbulent viscosity, μ_t, is expressed as

$$\mu_t = \rho L_s^2 \frac{\left(S_{ij}^d S_{ij}^d\right)^{3/2}}{\left(\overline{S}_{ij}\overline{S}_{ij}\right)^{5/2} + \left(S_{ij}^d S_{ij}^d\right)^{5/4}}. \tag{15}$$

Here, ρ represents the density, L_s denotes the mixing length for subgrid scales, S_{ij}^d is the modified rate-of-strain tensor, S_{ij} corresponds to the resolved rate-of-strain tensor, and $\overline{S}_{ij}$ is the rate-of-strain tensor for the resolved scale. These are given by

$$S_{ij}^d = \frac{1}{2}\left(\overline{g}_{ij}^2 + \overline{g}_{ji}^2\right) - \frac{1}{3}\delta_{ij}\overline{g}_{kk}^2, \tag{16}$$

$$\overline{g}_{ij} = \frac{\partial \overline{u}_i}{\partial x_j}, \tag{17}$$

$$\overline{S}_{ij} = \frac{1}{2}\left(\frac{\partial \overline{u}_i}{\partial x_j} + \frac{\partial \overline{u}_j}{\partial x_i}\right). \tag{18}$$

The mixing length, L_s, in the WALE model is determined using

$$L_s = \min\left(\kappa d, C_w V^{1/3}\right). \tag{19}$$

Within this equation, κ represents the von Kármán constant, d is the distance to the closest wall, C_w stands for the WALE constant (with a default value of 0.325), and V denotes the volume of the computational cell.

2.5. Cavitation erosion modeling

To examine the effect of the cavitation erosion, four variables are tracked in each time step. These variables are pressure (P), material derivative of pressure divided by cell volume $(DP/Dt)/V_{cell}$, square of material derivative of pressure $(DP/Dt)^2$ and second derivative of potential power density ($PPD2$). For the effective analysis of these variables, a User-Defined Function (UDF) implementing two algorithms, MAX1 and MAX2, is utilized. The MAX1 algorithm focuses on identifying the maximum value of the tracked parameters, providing a simplified yet insightful view into the peak conditions that may lead to erosion. Conversely, the MAX2 algorithm offers a more nuanced approach, considering the prevention of the fake collapses due to the surrounding cells and applying specific criteria to identify potential cavitation collapse cells [32,43]. This dual-algorithm approach enables a robust examination of cavitation phenomena, offering insights into both the instantaneous and evolving conditions that contribute to erosion.

2.5.1. Tracked variables

The following four indicators are tracked during the simulations:

1. Pressure (scaled with V_{cell}/V_{ref}): This variable represents the pressure within the system, scaled with the ratio of the cell volume to a reference volume (V_{ref}). The scaling is performed to eliminate the linear dependency of maximum pressure on the local cell size, as suggested by [4]. This approach ensures that the pressure values are independent of grid resolution, enabling consistent comparisons across simulations with varying mesh configurations.
   The reference volume V_{ref} is defined as the smallest cell volume in the computational domain. This choice ensures a stable and consistent scaling factor across the domain, particularly when refining the mesh or performing grid sensitivity studies. While V_{ref} is somewhat arbitrary, it remains constant for all simulations in this study, ensuring that relative comparisons of erosion metrics are unaffected by changes in mesh resolution. It should be noted that altering V_{ref} would proportionally change the scaled pressure values. Therefore, care has been taken to keep this reference volume consistent across all design iterations and configurations, as highlighted in [32].
2. $(DP/Dt)/V_{cell}$: This variable quantifies the material derivative of pressure divided by the cell volume itself. The material derivative provides insights into the rate of change of pressure over time, offering valuable information about the occurrence and intensity of cavitation erosion. The material derivative is defined as
   $$\frac{DP}{Dt} = \frac{\partial P}{\partial t} + U \cdot \nabla P. \tag{20}$$
3. $(DP/Dt)^2$: This variable represents the square of the material derivative of pressure, reflecting the magnitude of pressure fluctuations. Monitoring the squared material derivative helps us understand the intensity and rapid changes in pressure, which are linked to cavitation erosion.
4. $PPD2$: It measures the second derivative of potential power density, indicating the rate of change of power density with respect to pressure. This variable provides insights into the energy transfer and potential for damage caused by cavitation erosion and is given by [22]
   $$PPD2 = \left(p_v - P\right)\frac{\rho}{\rho_l - \rho_v}\nabla \cdot \mathbf{U}\ . \tag{21}$$

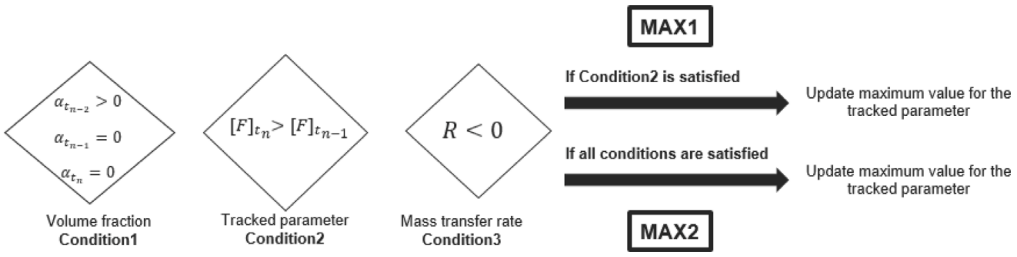

Fig. 1. MAX1 and MAX2 algorithms.

Table 4
Description of the variables in MAX1/MAX2 algorithm.

Description	Value
Tracked parameter at current time step	F_{t_n}
Tracked parameter at previous time step	$F_{t_{n-1}}$
Volume fraction of current time step	$\alpha_{t_{n-}}$
Volume fraction of previous time step	$\alpha_{t_{n-1}}$
Volume fraction of two previous time step	$\alpha_{t_{n-2}}$
Mass transfer rate at current time step	R_{t_n}

2.5.2. Tracking methodologies: MAX1 and MAX2 algorithm

There are two sets of algorithms, MAX1 and MAX2, implemented. The MAX1 algorithm is studied by previous researchers [19,21]. For this, only the maximum value of the tracked parameter (Table 4) is considered. The MAX2 algorithm relies on a prevent mechanism of fake collapses. The idea has been first introduced by Mihatsch et al. [43] and has been reformulated by Mouvanal [32]. Both of the algorithms loop over all cells at the end of each time step.

In particular for the MAX2 algorithm, there are 3 conditions that need to be satisfied to determine the cell as the "collapse cell". These conditions are shown in Fig. 1.

The first condition is necessary to distinguish whether there are transported vapor clouds from neighboring cells or if they are generated locally. Moreover, collapse due to rebound is particularly examined with a zero vapor volume fraction . This procedure has been first used by Mihatsch et al. [43] with a density-based solver. The second condition is checking the tracked parameter value of the current time step with the previous time step, with the physical insight that a collapse will occur with a higher tracked parameter value. Mouvanal [32] set this tracked parameter as pressure solely. In this study, additional tracked parameters ($(DP/Dt)/V_{cell}$, $(DP/Dt)^2$ and $(PPD2)$) are introduced alongside with the pressure (P). Finally, the third condition ensures that a condensation happened in that cell. Once these 3 conditions are satisfied in that loop, the maximum value for the each tracked parameter is updated within a cell loop that works at the end of each time step using the UDF.

2.6. Geometry and computational domain

Geometry modeling is an important phase for CFD simulations. The Computed Aided-Design (CAD) models offer design flexibility and simplification but may not capture real-world physics, while the Tomography Scan (TS) models provide a high-fidelity representation with details of the actual manufactured geometry. Both the CAD and TS models are provided by Woodward L'Orange. The models are represented in Fig. 2, and include 8 holes as the default configuration. It is clear from the provided figure that the surface deviations are especially noticeable in the injector orifice holes, which are prone to cavitation erosion in the high lift condition.

The numerical simulations are first divided into two main categories: CAD model and TS model. These simulations aim to provide a comprehensive understanding of the differences in cavitation erosion behavior in the presence of surface deviations. Computational domains are generated as 1-hole for the CAD model (Fig. 3(c)), while for the TS model both 8-hole (Fig. 3(a)) and 1-hole (Fig. 3(b)) domains are generated. The purpose of the 8-hole simulations of the TS model is to examine the cavitation erosion performance of each orifice individually, investigate differences between the orifices, and check for interactions between holes.

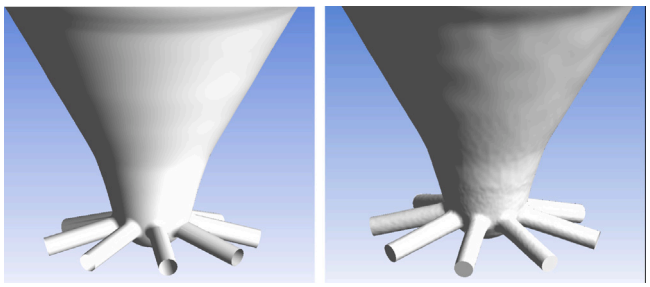

Fig. 2. CAD model (left) and TS model (right) comparison.

Considering the cost and time requirements, LES has been employed only for 1-hole computational domains. To provide a consistent comparison with LES simulations, the same computational domains are also analyzed with the RANS approach.

Fig. 4 presents the surface deviation of the TS model compared to the CAD model when both models in Fig. 2 are overlapped and aligned in the center. These contour plots are generated with the GOM Inspect 2022 software [44]. The focus was on analyzing surface deviations, particularly in relation to the orifices' entry dimensions and top/bottom downstream sections.

In general, the top side of the orifices exhibited a positive deviation, while the bottom side showed a negative deviation. These dimensional properties play a crucial role in the generation of cavitation, making this observation particularly significant. The examination further indicated that the entrance diameters of the orifices deviated up to 0.02 mm, positively on the top side and negatively on the bottom side. It is also clear to see that each orifice has different surface deviations and orifice entrance dimensions when they are compared with each other. This is another motivation to analyze TS model with 8-hole configuration using the RANS approach.

Fig. 5 illustrates the selected 1-hole, providing a top view of the TS model 8-hole geometry with hole numbering, and a bottom view from the geometry modeler. The upstream seating surfaces exhibit surface deviations, making it more challenging to maintain consistent topology

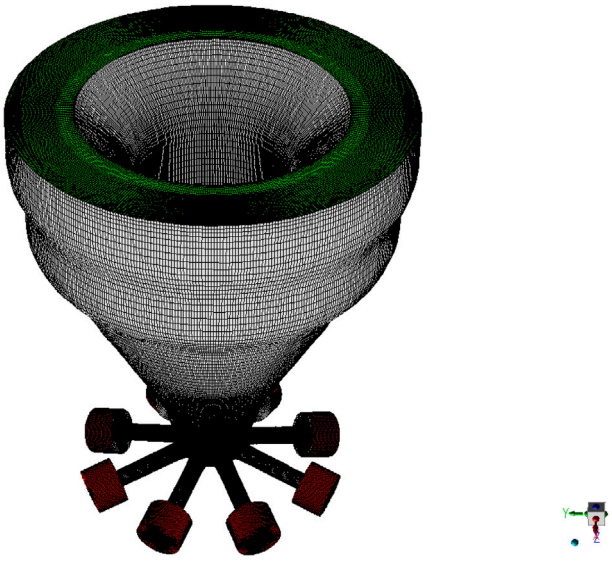

(a) TS model 8-hole , ∼11 million cells.

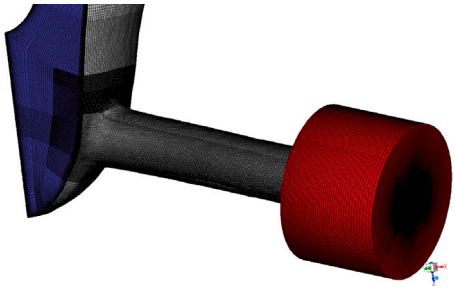

(b) TS model 1-hole , ∼9 million cells.

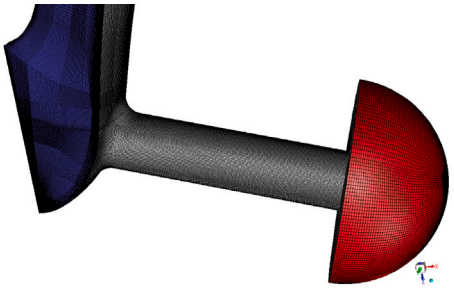

(c) CAD model 1-hole , ∼5 million cells.

Fig. 3. Computational domains with their cell count.

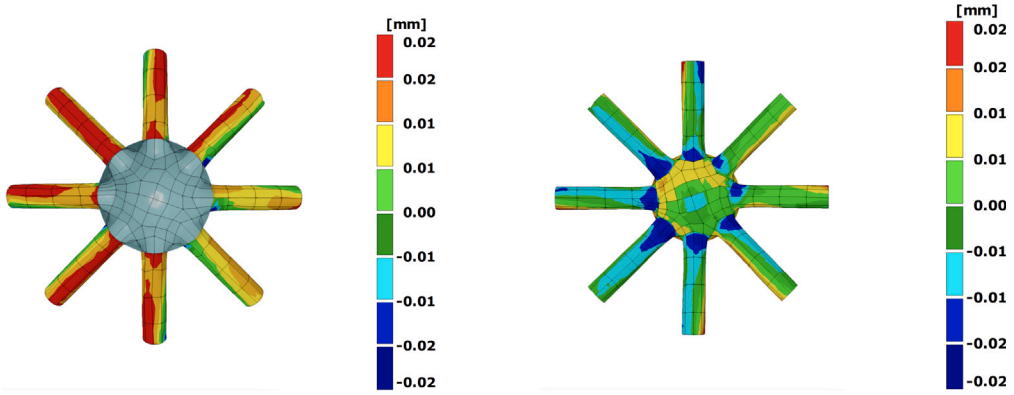

Fig. 4. Surface deviations between TS and CAD model injector holes. Top view (left), Bottom view (right).

and mesh periodicity. Therefore, 'hole7' was chosen as it presents fewer issues compared to the other holes.

The computational grid should have sufficient quality due to the spatial resolution requirement of LES. While several methods exist to assess grid quality for LES [45,46], these are typically used for non-cavitating flows. Celik's Index Quality [47] provides a more suitable measure for cavitating LES simulations because it accounts for multi-phase effects by having the information of the laminar mixture viscosity (μ) and turbulent mixture viscosity (μ_t). In this study, both Celik's Index Quality and Taylor length scale calculation are both used for the assessment of grid. It is suggested that by Celik et al. [47] that $LESIQ_v$ of 75% to 85% can be considered adequate for most engineering

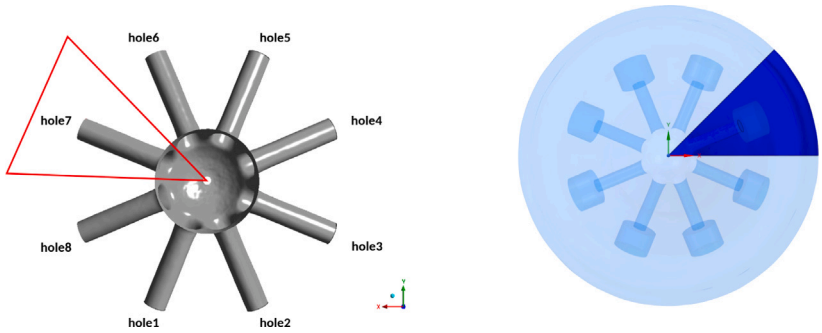

Fig. 5. Selected hole representation with top and bottom view to the TS model 8-hole geometry.

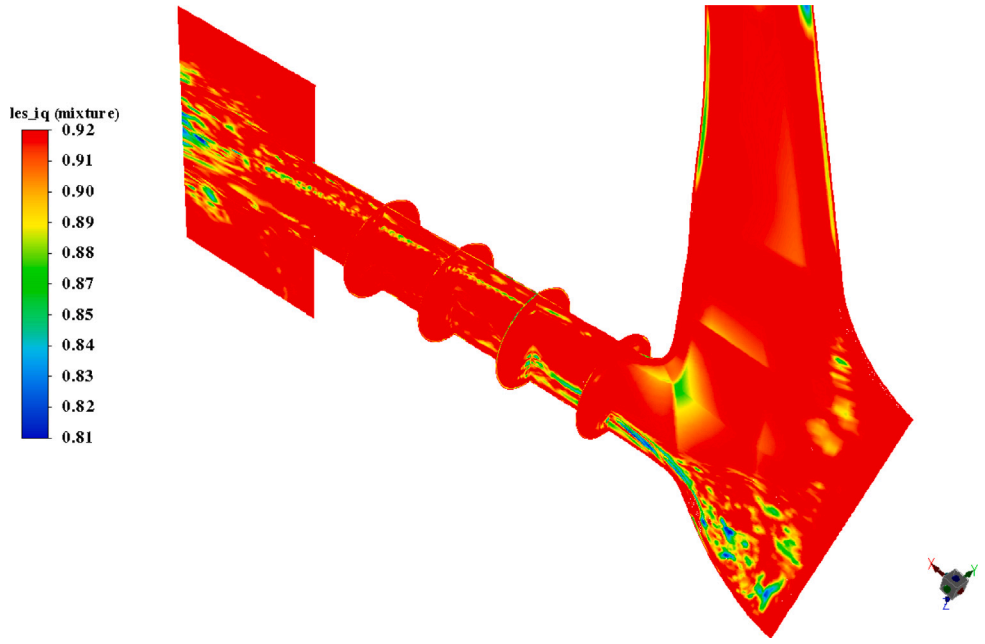

Fig. 6. Assessment of the grid (TS model 1-hole) with $LESIQ_v$ in various cut planes.

applications, where

$$LESIQ_v = \frac{1}{1 + 0.05\left(\frac{\mu+\mu_t}{\mu}\right)^{0.053}}. \quad (22)$$

The above equation is used as a post processing parameter to asses the quality of the grid. So, the computational grid has been analyzed (Fig. 6) both globally and locally with several cut planes via the $LESIQ_v$ parameter. It can be seen from Fig. 6 that the global minimum $LESIQ_v$ value is ~0.81, which lies within the acceptable range (75% to 85%) for LES as suggested by Celik et al. [47]. This indicates that the grid quality is sufficient for LES simulations.

The Taylor length scale, calculated using the equation $\lambda_g = \sqrt{10}\,\mathrm{Re}^{-0.5}L$, was taken into account for mesh refinement in different regions of the injector. The characteristic length, L, represents the relevant physical dimension of each region, such as the orifice diameter, needle seat distance, and average length of the sac volume, which are critical for scaling flow properties. The velocities listed in Table 5 are the time-averaged velocities within each specific region. These mean velocities are used to calculate Reynolds numbers and Taylor length scale across different injector zones. The values, as shown in Table 5, indicate the extent of refinement needed to capture the essential flow dynamics within each region, namely the needle seat, sac volume, and orifice.

Flow through the geometry is driven via pressure boundary conditions with a purpose of matching experimental conditions. 2200 bar total pressure is set at the inlet, which behaves like a subsonic reservoir boundary condition. Fluctuating velocity at the inlet is not considered, since it does not have any effect on the overall flow field [48]. 10 bar static pressure is given at the outlet surface. It should be noted that the

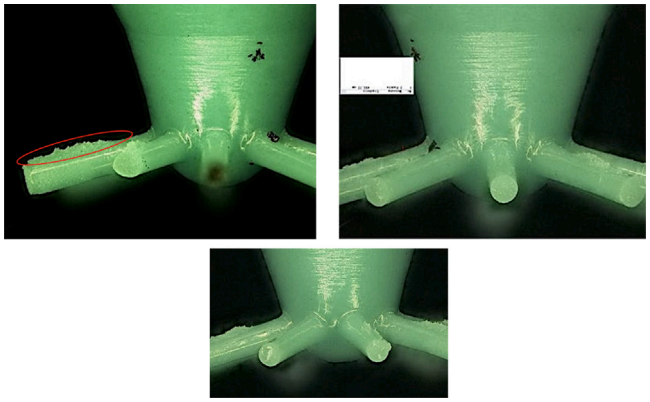

Fig. 7. Experimental images for the high lift condition (480 μm), showing epoxy-filled geometry to highlight eroded material.

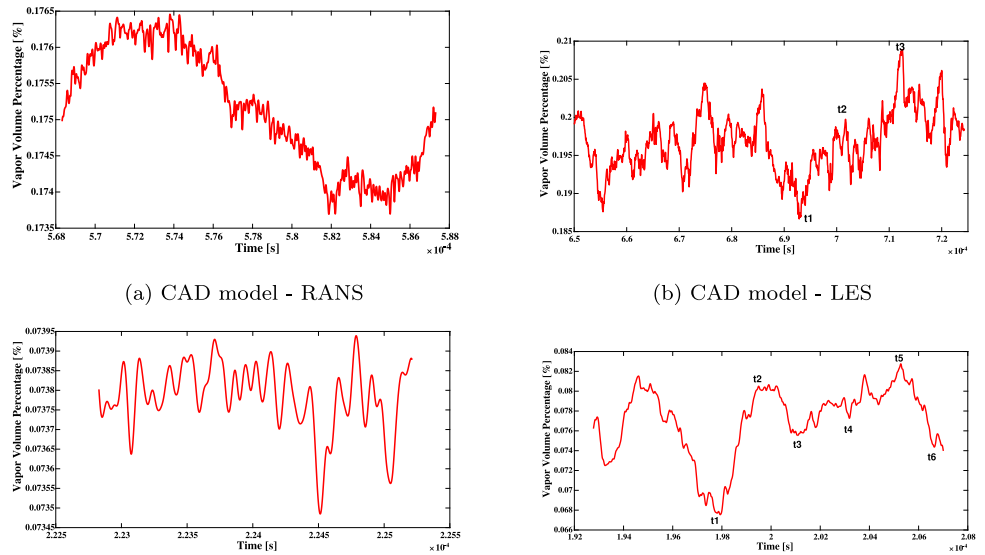

(a) CAD model - RANS (b) CAD model - LES

(c) TS model - RANS (d) TS model - LES

Fig. 8. Total vapor volume change of 1-hole simulations.

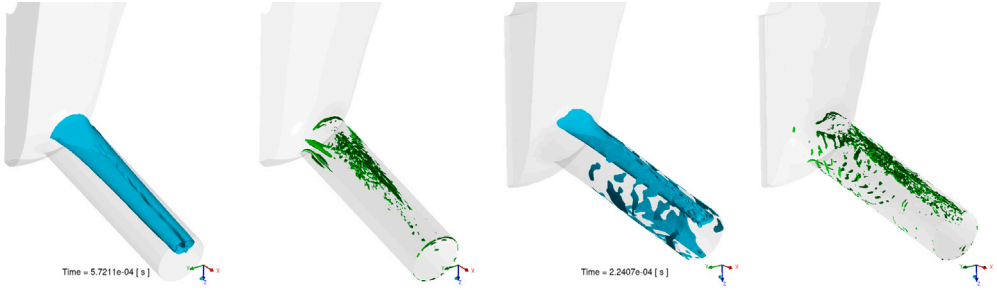

(a) CAD model - RANS (b) TS model - RANS

Fig. 9. Vapor formations (α = 0.5) and turbulent structures ($\lambda_2 = 5 \times 10^{13}$).

Table 5
High lift condition.

	Characteristic Length (m)	Velocity (m/s)	Reynolds Number	Taylor Length Scale (m)
Needle Seat	4.8×10^{-6}	200	35 000	5×10^{-6}
Sac Volume	~0.0008	200	55 000	4×10^{-6}
Orifice	0.0003	700	70 000	3×10^{-6}

computational domain is extended from the orifice exit to a slightly more downstream position, and outlet ports located at the end of this extension. This extension aims to mitigate the impact of outlet pressure on the upstream flow field. Additionally, during the simulations, cavitation formations have been observed reaching up to the orifice exit.

To reduce the computational cost, the 1/8 portion of the entire injection system is modeled for 1-hole only simulations. Periodicity is provided with periodic boundary conditions that are applied on the side surfaces. Boundary conditions are also represented with different colors in Fig. 3.

2.7. Numerical setup

The simulations are performed with the Ansys Fluent CFD solver. The pressure-based formulation has been used for all studies. Pressure and Velocity are coupled with "Coupled" algorithm, which is known as more robust compared to the segregated algorithms [39]. The pressure equation is discretized with the "Body Force Weighted" scheme, while for the momentum equations "Bounded 2nd Order" numerical scheme is used. 2nd Order Upwind scheme is applied to the density, volume fraction and turbulent scalars transport equations. Time is discretized with the 2nd order implicit formulation for RANS, and the bounded 2nd order implicit formulation for LES.

A residual convergence of 1×10^{-5} for all flow variables was achieved within a maximum of 50 inner iterations. Additionally, the mass transfer rate was used as an extra convergence control parameter, requiring a minimum convergence value of 1×10^{-5} at each time step. Additional simulations were also conducted with a higher convergence criteria of 1×10^{-8} for all flow variables. However, these simulations did not produce any significant differences in the results.

The adaptive time stepping is applied by limiting the CFL number to 2 for RANS and 1 for LES simulations. This leads to varying time step

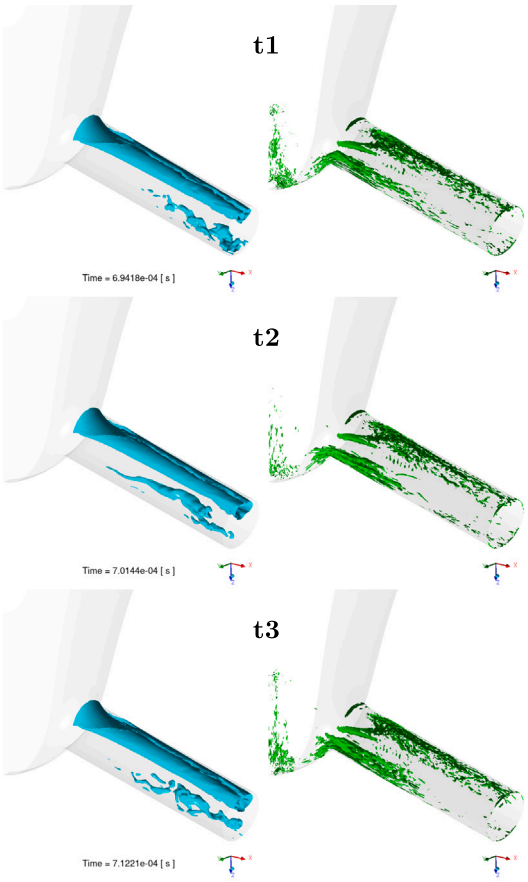

Fig. 10. Vapor formations (α = 0.5) and turbulent structures ($\lambda_2 = 5 \times 10^{13}$) t1, t2, t3 – CAD model – LES.

around 2 ns for RANS and 1 ns for LES simulations. All flow statistic has been collected at least 5 flow-throughs for each simulation after the initial washout/transients disappeared.

3. Test case and experiments

Experiments were performed on a high-pressure injector from Woodward L'Orange, typically used in heavy-duty and marine engines. This injector operates under a pressure of 2200 bar, and features 8 holes designed for optimum fuel delivery. The experiment, conducted at Woodward L'Orange facilities, was performed under a static high lift condition, 480 µm. Fig. 7 shows photographs taken at the end of the high lift experiment. Here, the geometry is filled with an epoxy material, which fills gaps of the eroded material. The experimental images suggest that material removal occurs predominantly on the upper side of the injector holes. However, it is important to note that the bottom side of the injector was not captured clearly in the photographs.

Although the experiment has been done with fixed lift positions, different erosion patterns are obtained when the injector holes are compared. These discrepancies are thought to be linked with,

- Center position mismatch of the needle within the sac due to machinery vibrations and/or incorrect positioning; and
- Having different surface deviation of each hole. This is going to be discussed in more detail in upcoming sections.

While evaluating cavitation erosion experiments, it is important to note that the initial geometry becomes invalid once material removal begins. Therefore, it is crucial to exercise caution when comparing computational fluid dynamics (CFD) results with experimental results, as there are no geometry changes that occur during the calculations.

4. Results and discussion

This section presents the numerical simulation results and their analysis. Initially, the statistics and flow field characteristics are examined, including temporal vapor volume changes and visualizations of vapor formations and turbulent structures. Comparative analysis between RANS and LES models using CAD model and TS model geometries highlights differences in cavitation behavior and turbulence dynamics. Subsequently, an erosion assessment is performed for each simulation configuration using the aforementioned indicators and algorithms to identify potential damage zones within the injector orifice.

4.1. Flow field

The vapor volume percentage represents the ratio of the vapor phase volume to the total volume of the fluid mixture in a specific region of the injector, and given by,

$$\text{Vapor volume percentage} = \left(\frac{V_{\text{vapor}}}{V_{\text{total}}} \right) \times 100, \tag{23}$$

where V_{vapor} is the volume of the vapor phase, and V_{total} is the total volume of the mixture (vapor + liquid).

The vapor volume percentage change in time for all 1-hole configurations are presented in Fig. 8. Here, in Fig. 8(a), CAD model — RANS shows a low magnitude oscillatory pattern in vapor volume throughout the selected time interval. This type of locally dynamic cavitation process is mainly due to the attached sheet cavity on the top side of the injector. This vapor formation is presented with volume fraction (α) iso-vapor surfaces in Fig. 9(a) (left) alongside with the turbulent structures (right), created by iso-surfaces of λ_2 criterion, a method to identify and visualize vortical structures within a flow field [49]. It is clearly seen that the attached sheet cavity is split into two cores, as observed by the previous studies [50,51] in similar conditions. Here, the vapor starts to form near the orifice inlet due to the surface curvature and it has an overall smooth shape except the region where coherent turbulent structures exist in more downstream position of the inlet and extends to the middle of the orifice. There are also turbulent structures on the bottom side of the orifice inlet, but these are not strong enough to create low pressure regions, and thus not cavitation.

The CAD model — LES, plotted in Fig. 8(b), exhibits a more random pattern in the vapor volume change over time compared to the CAD model — RANS, which is in line with the ability of the LES model to capture larger and more dynamic range of eddies and flow structures. The significant difference between global minimum (t1) and maximum (t3) suggests the presence of additional cavitation structures. The transient nature of cavitation and its interaction with the turbulent flow within the injector is shown in Fig. 10 for three time instants (t1, t2, t3). As observed in Fig. 8(b), overall vapor structures show more dynamic behavior, unlike the CAD model — RANS results. On the bottom half of the orifice, vortex cavitation is present and it grows and changes its shape over time. This structure was not present in the CAD model — RANS results. The general form of the top side vapor formation is almost similar with CAD model — RANS, hence it is split into two parts. The attachment region surface between the attached sheet cavity and (top side) orifice wall shows more intermittent behavior as the flow progress as in downstream position. Turbulent structures (λ_2 criterion) on the right side of Fig. 10 reveals more information about the attached cavity region. High shear activity in that region between the vapor and liquid is present in all time instants. Besides that there are two additional turbulent structures visible: One is in the orifice bottom side near inlet which is mainly responsible of generating the bottom side vapor structures by creating low pressure regions. The other one stays inside the sac region and is basically a part of the re-circulation region, which

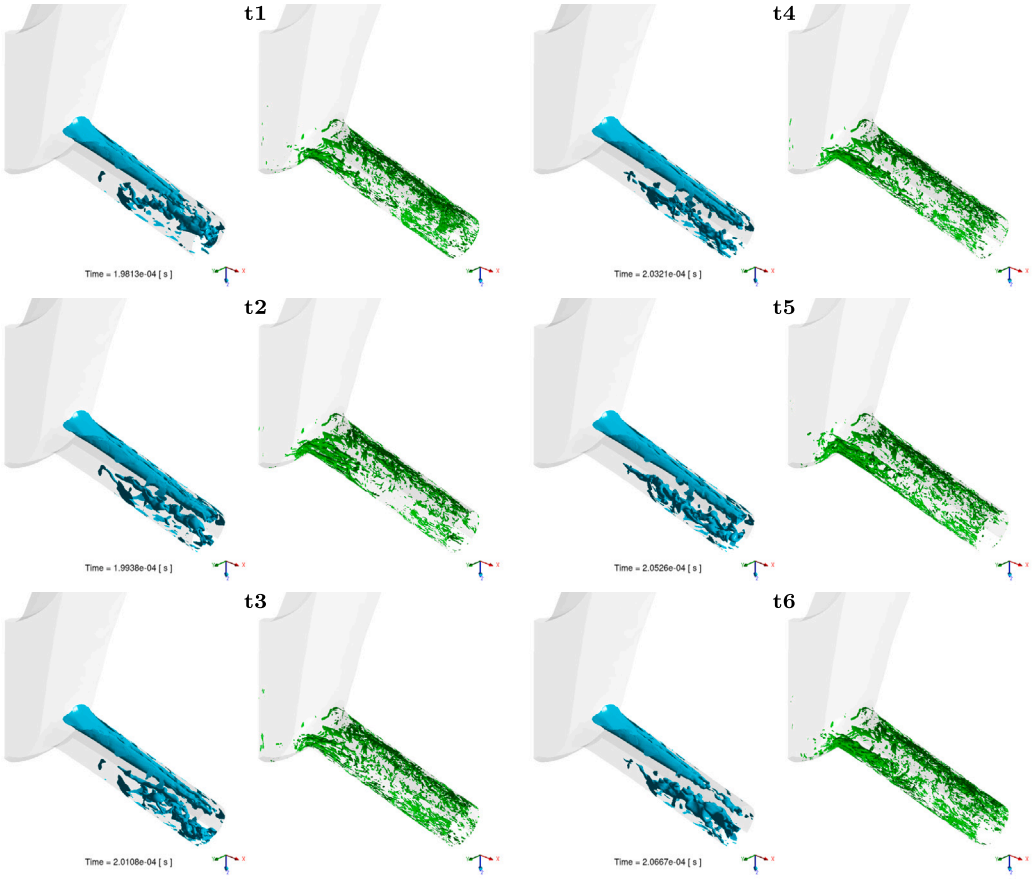

Fig. 11. Vapor formations (α = 0.5) and turbulent structures ($\lambda_2 = 5 \times 10^{13}$) t1–t6 – TS model – LES.

is more clearly seen with a streamline representation from the right side of Fig. 12(a). On the left side of this figure, high vorticity regions correlate with zones of intense turbulence and cavitation structures. The transient behavior observed in LES simulations, with distinct vortex cavitation and attached sheet cavitation regions, aligns with findings by Kolovos et al. [16] and Falsafi et al. [17]. These studies highlight LES's ability to resolve small-scale turbulence and capture cavitation dynamics.

The vapor volume percentage change in time for the TS model is plotted in Fig. 8(c) and in Fig. 8(d) for RANS and LES, respectively. For TS model — RANS, the data is presented with a short duration to show the intermittent changes in simulation. The average vapor volume percentage is 0.0735%, while for the CAD model this value was around 0.175%. Hence, there is a reduction in total vapor volume once the surface deviation features are taken into account in the TS model. A further insight is provided by Fig. 9(b), where the presence of additional vapor structures due to surface deviations is evident. A direct comparison with the RANS CAD model indicates a reduced volume of the attached sheet cavity at the top side of the injector in the TS model. This reduction is apparent on the left side of Fig. 9(b), where the sheet cavity begins at the orifice inlet and extends to the outlet, but is narrower throughout the flow path. The turbulent structures on the right side of Fig. 9(b) show that small turbulent structures (near the orifice sides) can be directly created by surface deviations. Compared to the CAD model — RANS results, the TS model exhibits higher turbulent activity on the top side of the orifice, with turbulent structures extending up to the orifice exit.

For the TS model — LES (Fig. 8(d)), the average vapor volume percentage here is 0.075%, while in the CAD model — LES results this value was around 0.2% . The global minimum (t1) and maximum (t5) values are also less than the CAD model — LES results. It has been explained in the previous paragraph that this is due to the surface deviations.

Six selected (indicated and labeled in Fig. 8(d)) snapshots for the vapor and turbulent structures are presented in Fig. 11 with their corresponding time instants. Similarly as in previous results, cyan colored iso-surfaces show the vapor formations and turbulent structures are provided in the right side of the each time instant with green surfaces.

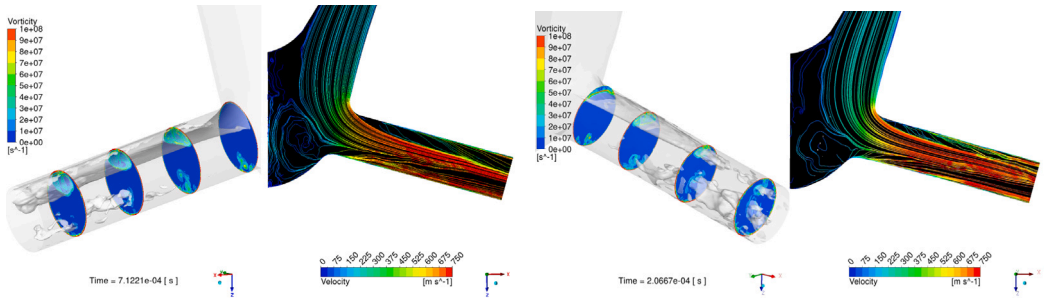

(a) CAD model - LES (b) TS model - LES

Fig. 12. Vorticity fields on cross section cut planes together with transparent vapor structures (left) and velocity colored streamlines on injector mid-plane (right).

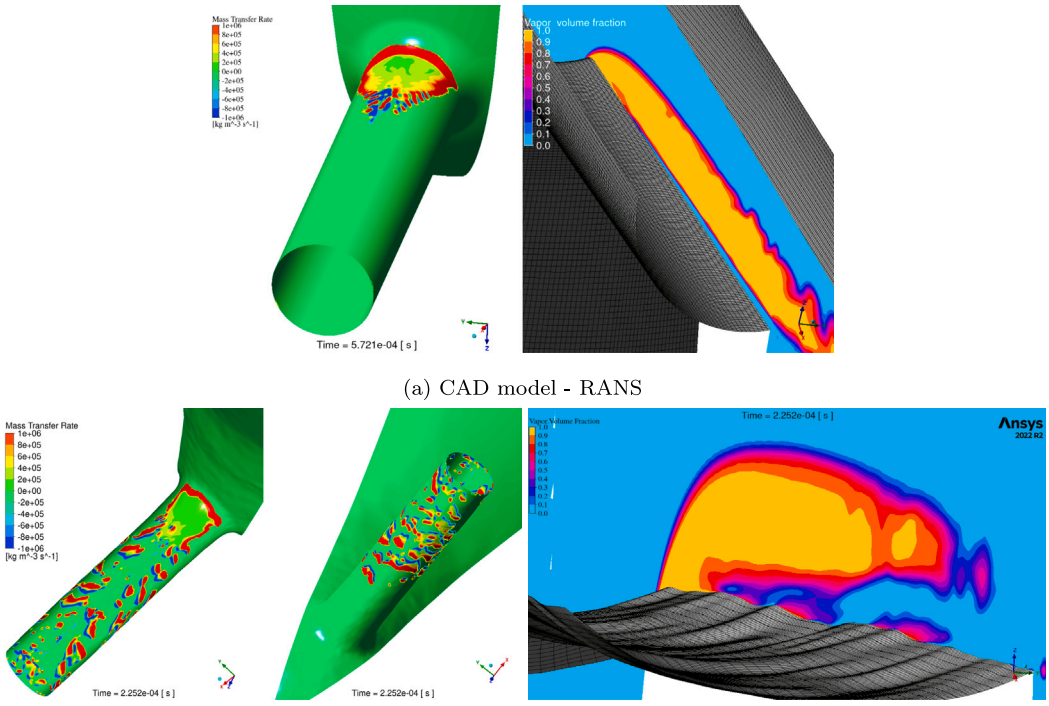

(a) CAD model - RANS

(b) TS model - RANS

Fig. 13. Surface mesh representation with cut plane volume fraction (right) and Mass Transfer Rate contour plot on the walls (left).

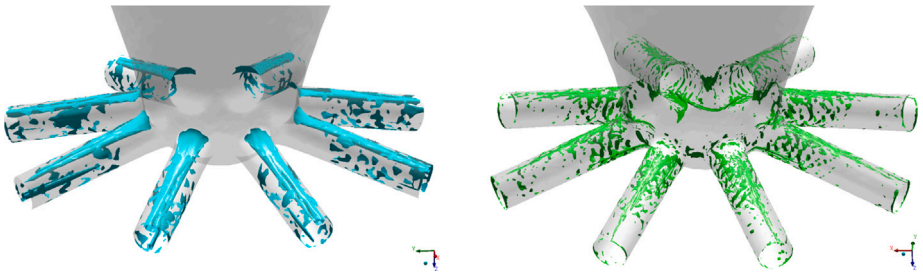

Fig. 14. Vapor formations (α = 0.5) and turbulent structures ($\lambda_2 = 5 \times 10^{13}$) – TS model 8-hole – RANS.

It is evident from the images of vapor structures at the t1 instant that the attached sheet cavity does not reach the orifice exit. At t1, the stream-wise length of the split two core vapor is shorter compared to what is observed in the subsequent time instants t2 to t5. From t5 to t6 the vapor volume gets condensated back to the liquid, hence collapses. Apart from the attached sheet cavity on the top side, vortex cavitation structure on the bottom half changes its shape through time t1–t6. For all time instants, the turbulent activity is high and turbulence

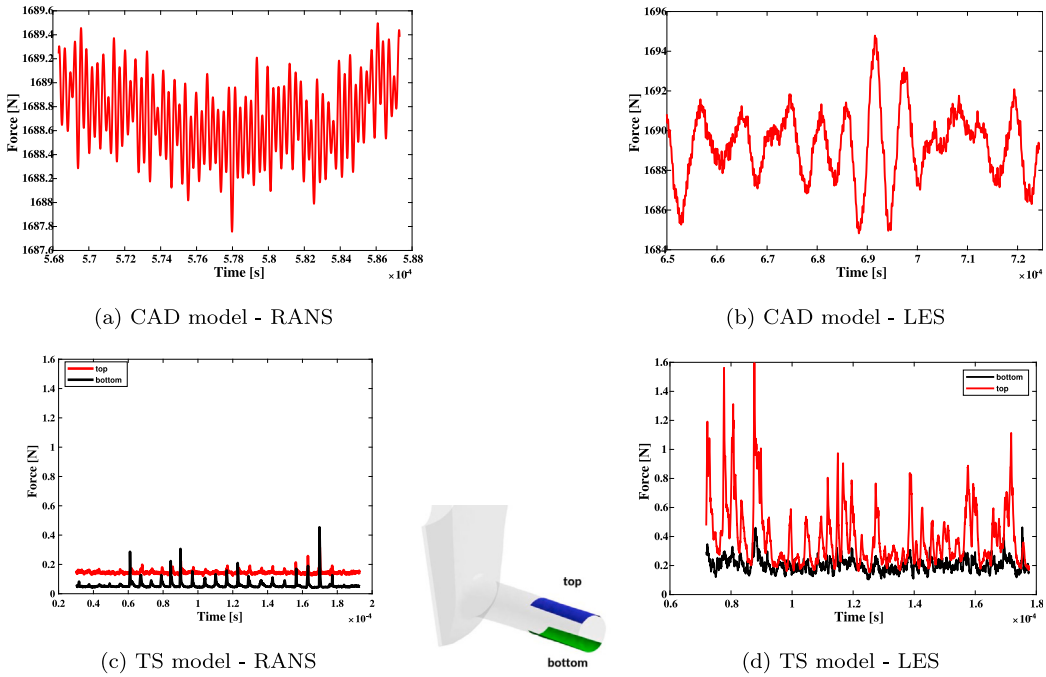

(a) CAD model - RANS (b) CAD model - LES

(c) TS model - RANS (d) TS model - LES

Fig. 15. Force plot comparison history of the selected "top" and "bottom" orifice surfaces.

generation due to the surface deviations are more visible compared with the TS model — RANS results 9(b). The turbulent structures near the bottom side of the orifice entrance persist and undergo changes in their overall shape over time. The size and number of the iso-surfaces increased from t1 to t2, then get back to its same size in t3. On the top side of the orifice high shear activity due the attached sheet cavity is apparent.

The time instant t6 is further examined in Fig. 12(b) with vortical structures and cut plane streamline to provide an insight about cavitation and turbulence relationship. Here on the left side, the presence of strong vortices enhance the cavitation process especially in the bottom half by lowering the pressure in that region. This interplay between turbulence and cavitation agrees with Koukouvinis et al. [19], who linked high shear zones to cavitation inception. Additionally, it is worth noting the vortices created by surface deviation near the exit of the orifice. On the right side, the flow is accelerating in the pure liquid region since the vapor structures are narrowing down the orifice hole passage transporting in lower velocity. Hence, the difference in velocity creates shear layer regions inside the orifice.

To further investigate the effect of the surface deviations solely in the presence of RANS, Fig. 13 presents spatial mass transfer rate distribution on the orifice walls and cut plane volume fraction together with the surface mesh representation of the CAD and TS model. The vapor generated near the orifice inlet in CAD model — RANS can be identified here (Fig. 13(a)) as well with red colored mass transfer rate contour values on the wall. In more downstream position, where the turbulent activity is high (see Fig. 9(a) — right), both vapor generation and condensation patterns are present. It is also clear from the cut plane volume fraction that the vapor is separated from the top side of the orifice and convected downstream. Whereas in Fig. 13(b), it is clearly evident from both mass transfer rate distribution and cut plane that surface deviations create additional vapor structures on the all sides of the orifice wall. This vapor generation mechanism is present across the whole orifice wall surfaces, unlike the CAD model — RANS.

In Fig. 14, vapor formations and turbulent structures snapshots are presented for the TS model 8-hole — RANS configuration. On the left side of Fig. 14, the overall shape of cavitation structures is similar, but characteristics of attached sheet cavity on the top side of the each hole may vary for some particular holes in downstream positions. Additionally, some holes have bottom half vapor formations, which are not captured in the TS model 1-hole — RANS simulations, only with LES turbulence modeling. On the right side of Fig. 14, it is possible to see hole to hole interactions between the holes. These hole-to-hole interactions are consistent with Örley et al. [15], who emphasized their importance in capturing complex flow phenomena. These interactions are not seen in the TS model 1-hole simulations, even with TS model — LES results. This might be due to the limitation of the periodic boundary conditions [15].

For any particular hole, the number of cells and level of resolution is different between TS model 1-hole and 8-hole simulations. To achieve the same level of mesh resolution in the 1-hole for the 8-hole simulation, a high cost is estimated that around 55 million cells are needed. Nevertheless, these results further points out the importance of hole to hole interactions and effect of each hole's identical surface deviations.

4.2. Force statistics

Before presenting the erosion assessment results, a force history plot of all the 1-hole configurations is shown in Fig. 15. For the CAD model simulations, the force data is collected across the entire injector walls (needle, needle seat, and orifice) and plotted in Figs. 15(a) and 15(b), for CAD model — RANS and CAD model — LES, respectively. For the TS model (1-hole) simulations, a force comparison is provided by the selected "top" and "bottom" orifice surfaces since the experiments suggest that the damage is higher on the top side.

The relative change in force for the CAD model — RANS is very small since the pressure integration surfaces covers the entire injector walls. Nevertheless, there are still unsteady dynamics visible, as also shown in Fig. 8(a). The CAD model — LES data in Fig. 15(b) displays more pronounced fluctuations with broader ranges compared to the

RANS results. The distinction mainly arises from having additional cavitation dynamics and vapor structures in the LES model. The presence of vapor formations along the wall creates regions of low pressure, which are reflected in the force calculations as low values. Conversely, when these vapor structures collapse, they result in high-pressure spikes.

The force comparison plot, provided in Fig. 15(c), for the "top" and "bottom" orifice surfaces shows the respective forces acting on these regions over time. The spikes in force could be indicative of cavitation bubble collapse events that exert impulse loads on the injector surfaces, leading to potential erosion. The variation between top and bottom forces also suggests an asymmetric distribution of cavitation within the orifice. Moreover, the consistent low amplitude of force on the bottom surface (except the spikes due to numerical artifacts) could be interpreted as a sign of less aggressive or less frequent cavitation occurrences, or possibly a more stable cavitation that does not result in strong impulsive loads. The presence of higher force magnitudes on the top surface indicates that this region is more prone to cavitation erosion and subjected to more severe cavitation events, due to impulsive behavior of the attached sheet cavity in that area.

Fig. 16 presents a sequence of snapshots depicting the collapse of vapor formations alongside corresponding pressure distributions on the top and bottom sides of the injector orifice over time for TS model — LES simulation. The selected time interval here is from t5 to t6 (in Fig. 8(d)). As the time progress, on the top side of the orifice, attached sheet cavity shrinks and collapse near the orifice outlet and create wall pressure with a magnitude of at least 200 bar. The bottom side vapor formation (vortex cavitation) on the other hand, does not create such an high wall pressure values although it changes its shape. The similar mechanism can be examined in Fig. 15(d), which provides the force history of selected "top" and "bottom" orifice surfaces for TS model — LES simulation. The sharp peaks, particularly on the top surface (red line), suggest moments when cavitation bubbles collapse near the wall, causing high-pressure impacts. These impacts can be strong enough to damage the material over time. The relative height and frequency of the peaks could indicate the severity and rate of cavitation events. Higher and more frequent peaks on the top surface suggest more intense cavitation erosion activity compared to the bottom.

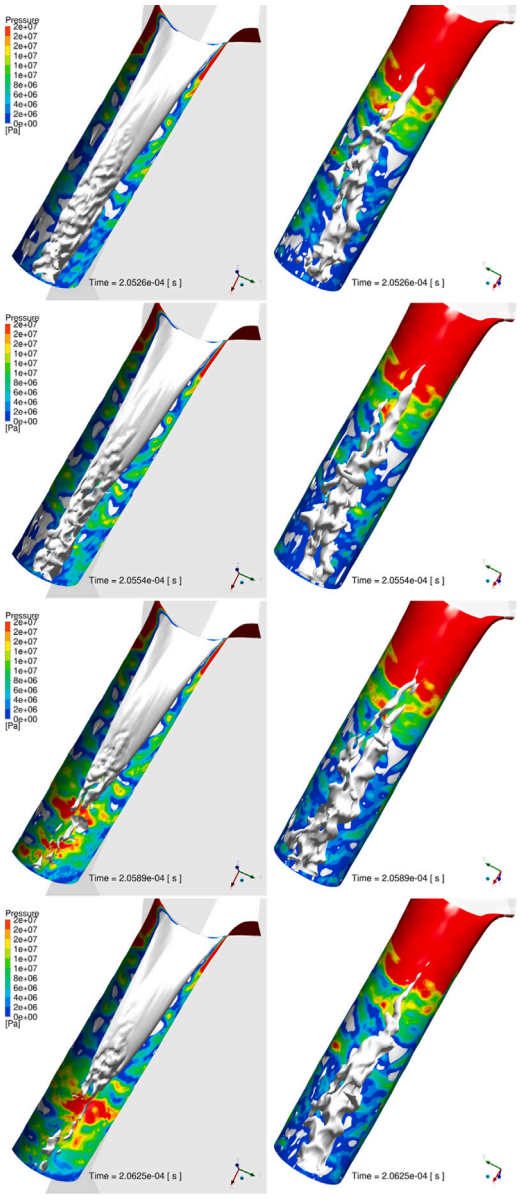

Fig. 16. Collapse mechanism representation with vapor formation and wall pressure snapshots on the top (left) and bottom (right) side of the orifice.

4.3. Erosion assessment

4.3.1. CAD model — RANS

Erosion assessment using the MAX1 and MAX2 algorithms are illustrated in Fig. 17. Here, it should be mentioned that a red colored region indicates a high risk of cavitation erosion. This information needs to be taken into consideration for the rest of the erosion assessment results.

The orifice entrance is the region where the flow encounters a reduced cross-sectional area relative to the upstream sac volume/cavity. While a simple constriction would normally accelerate the flow and reduce the pressure (as per Bernoulli's principle), in this specific region, the flow undergoes deceleration and a change in direction, leading to a local stagnation effect. Here, the kinetic energy of the fluid is converted into pressure energy, resulting in a rise in stagnation pressure at the orifice entrance. It is possible to see this stagnation pressure effect on all erosion indicators with the MAX1 algorithm in Figs. 17(a)–17(d), whereas for the MAX2 algorithm in Figs. 17(e)–17(h) this effect has been overcome with the help of the additional conditions in the MAX2 algorithm. Apart from this effect, for both algorithms, $(DP/Dt)^2$ and $PPD2$ erosion indicator patterns are located at the top side of the orifice as observed in high lift experiments (Fig. 7). However, the length of the erosion pattern in simulations is much shorter compared to the experiments.

4.3.2. CAD model — LES

Erosion assessment using the MAX1 and MAX2 algorithms are illustrated in Fig. 18. Stagnation effects are still present near the orifice entrance in the MAX1 algorithm for all erosion indicators, while for the MAX2, these effects are not present and cavitation erosion risk is more localized over the top and bottom of the orifice wall. Here, only the indicator "MAX2 P" (Fig. 18(e)) differentiate from the others by suggesting that the risk is higher on the top side than the bottom side of the orifice. In experiments, only the top side of the orifice is expected to be eroded along the orifice length. The extent of the erosion pattern in these results is much longer when compared with RANS results (Fig. 17(e)). Therefore, for this specific region, LES performs better than RANS. This result aligns with Falsafi et al. [17] and Magnotti [30], who showed that LES captures detailed cavitation-induced pressure spikes.

The bottom side erosion pattern for LES in both MAX1 and MAX2 is mainly due to the collapse of the vortex cavitation formations at the

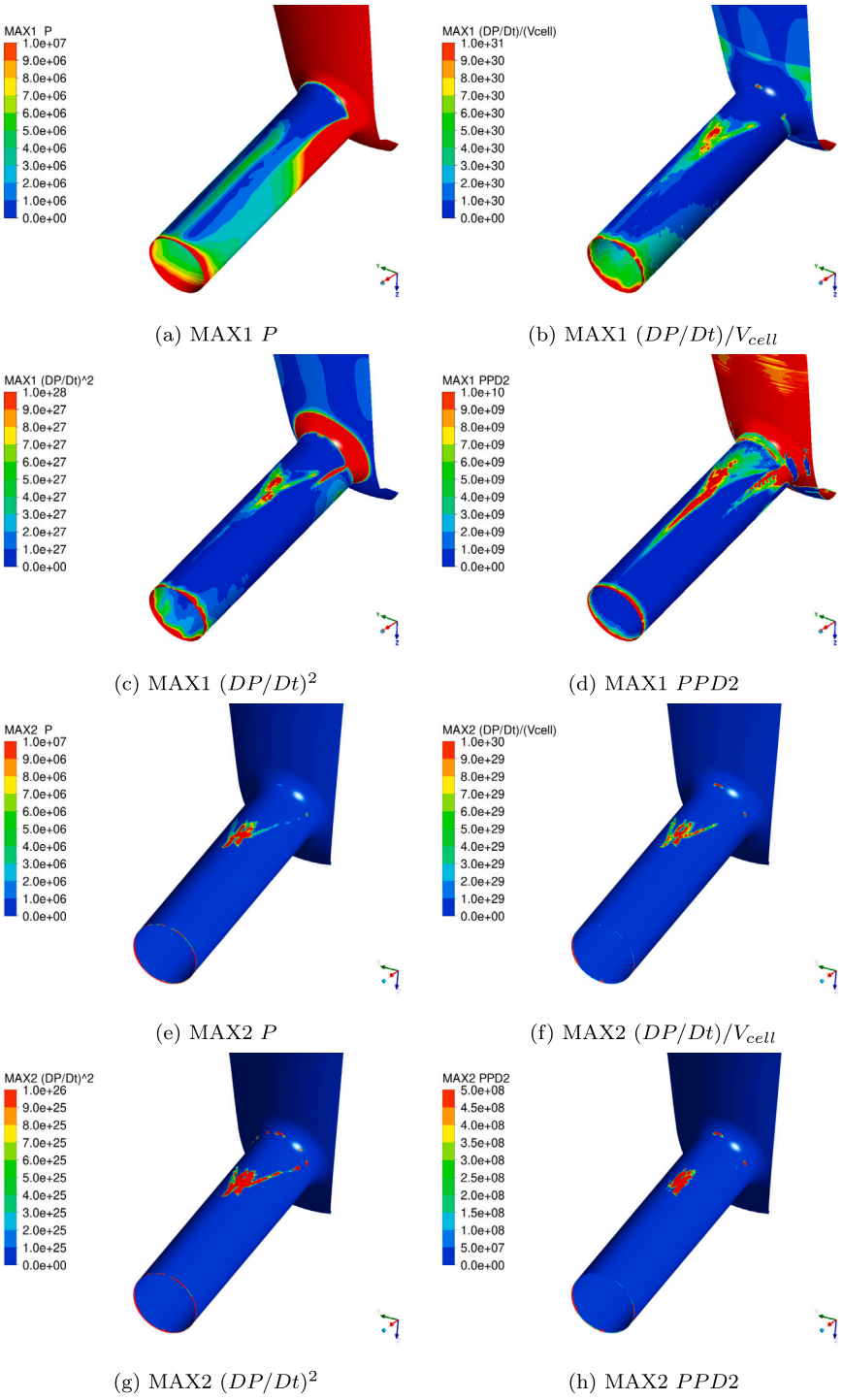

(a) MAX1 P (b) MAX1 $(DP/Dt)/V_{cell}$

(c) MAX1 $(DP/Dt)^2$ (d) MAX1 $PPD2$

(e) MAX2 P (f) MAX2 $(DP/Dt)/V_{cell}$

(g) MAX2 $(DP/Dt)^2$ (h) MAX2 $PPD2$

Fig. 17. Erosion assessment results – CAD model – RANS.

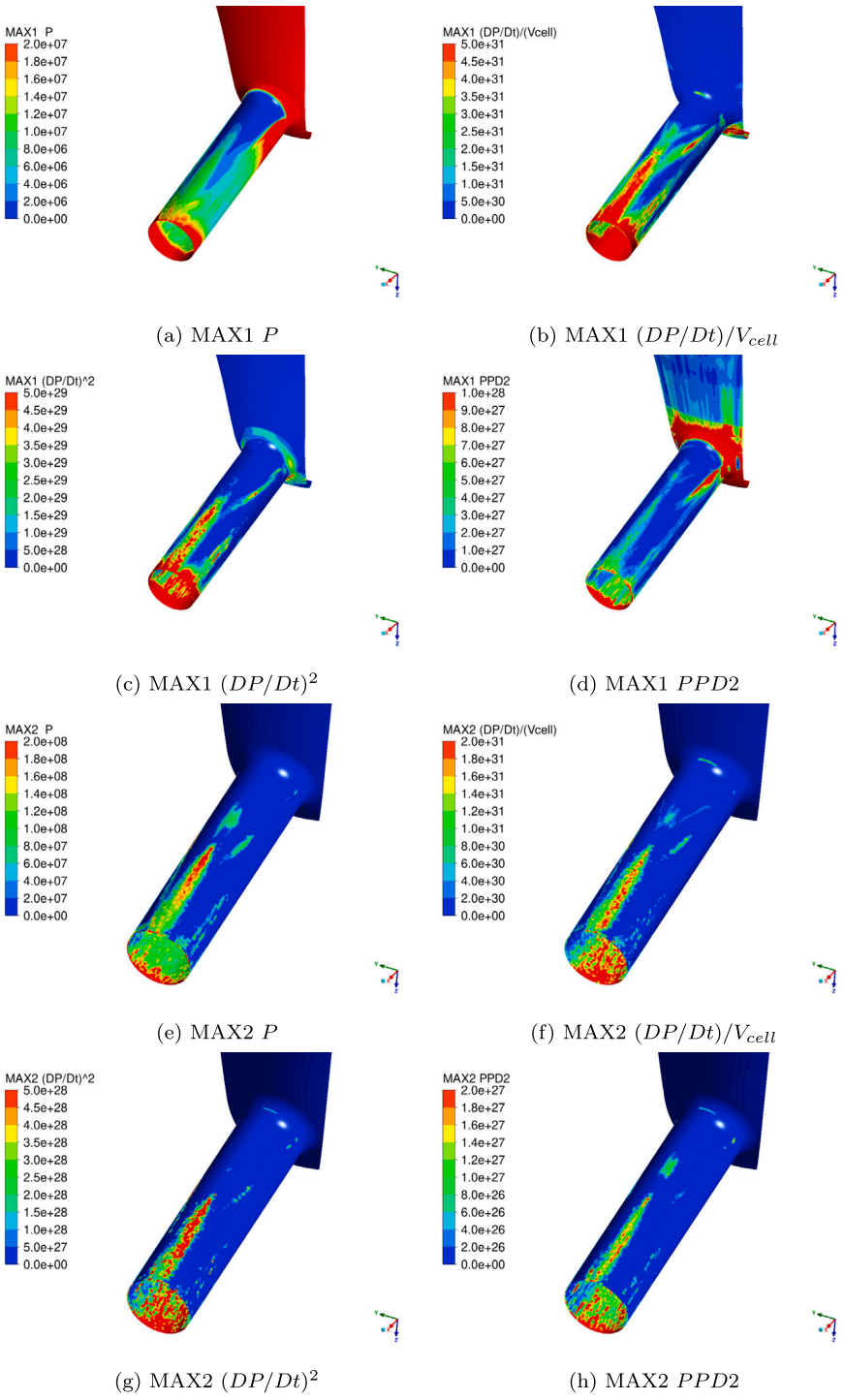

(a) MAX1 P (b) MAX1 $(DP/Dt)/V_{cell}$

(c) MAX1 $(DP/Dt)^2$ (d) MAX1 $PPD2$

(e) MAX2 P (f) MAX2 $(DP/Dt)/V_{cell}$

(g) MAX2 $(DP/Dt)^2$ (h) MAX2 $PPD2$

Fig. 18. Erosion assessment results – CAD model – LES.

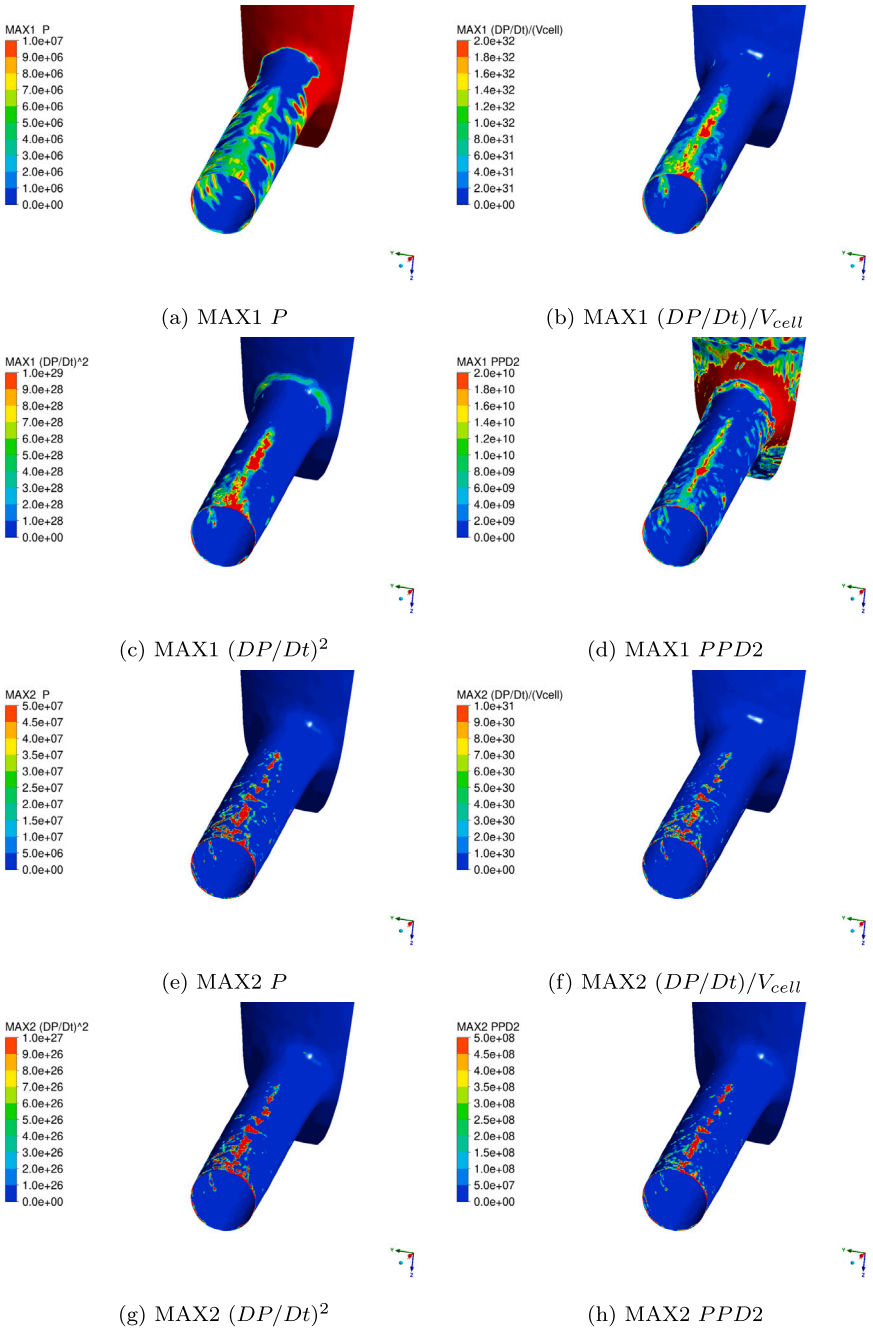

(a) MAX1 P (b) MAX1 $(DP/Dt)/V_{cell}$

(c) MAX1 $(DP/Dt)^2$ (d) MAX1 $PPD2$

(e) MAX2 P (f) MAX2 $(DP/Dt)/V_{cell}$

(g) MAX2 $(DP/Dt)^2$ (h) MAX2 $PPD2$

Fig. 19. Erosion assessment results – TS model – RANS.

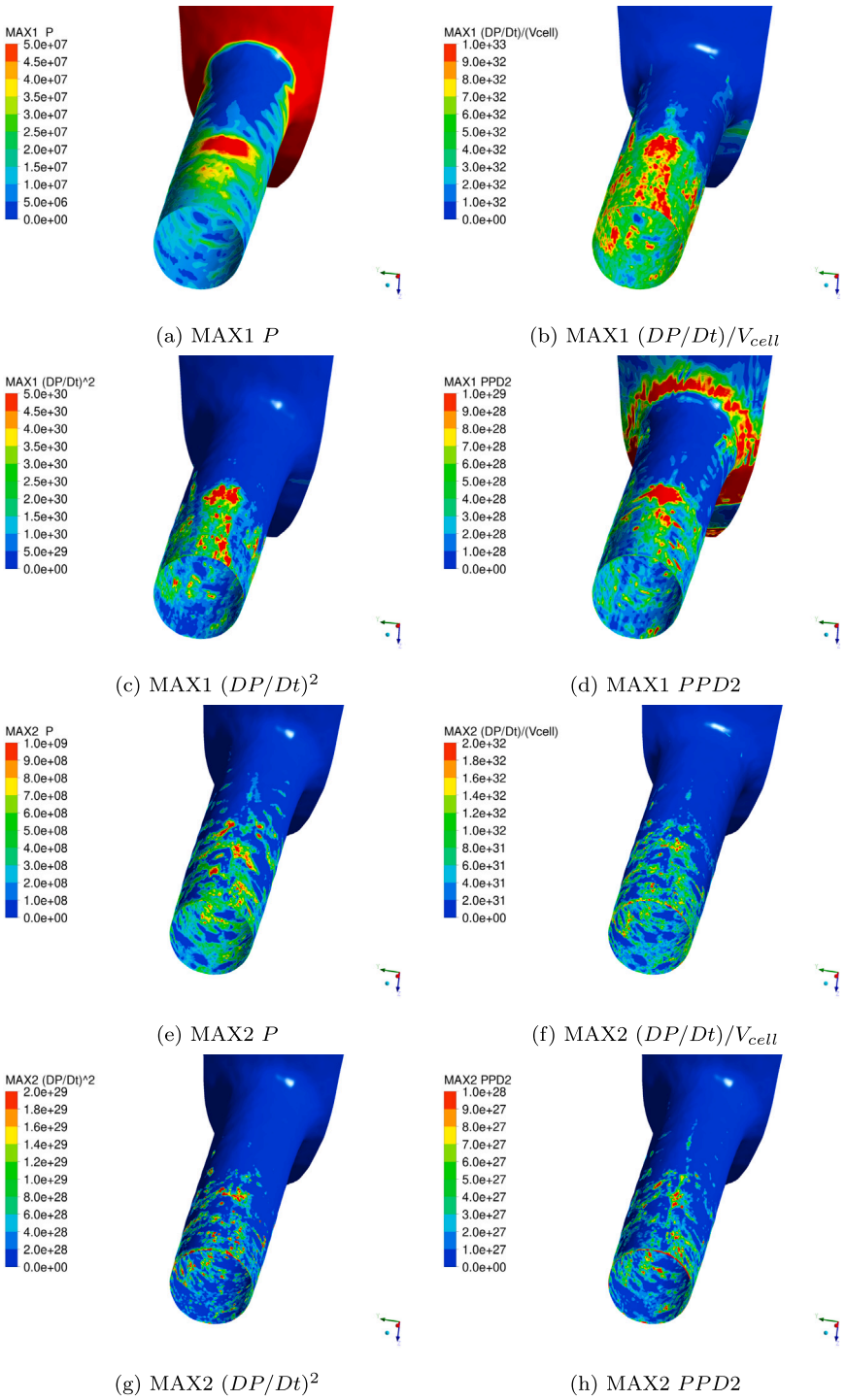

(a) MAX1 P (b) MAX1 $(DP/Dt)/V_{cell}$

(c) MAX1 $(DP/Dt)^2$ (d) MAX1 $PPD2$

(e) MAX2 P (f) MAX2 $(DP/Dt)/V_{cell}$

(g) MAX2 $(DP/Dt)^2$ (h) MAX2 $PPD2$

Fig. 20. Erosion assessment results – TS model – LES.

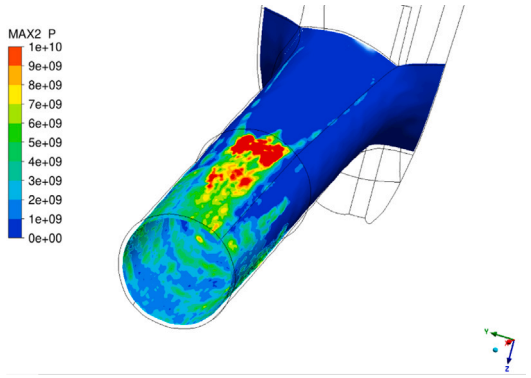

Fig. 21. Erosion assessment of 10 μm TS model offset surface — MAX2 *P*.

bottom half side of the orifice. There is no further information from the experiments if the bottom side vapor formation is physical or not. This will be elaborated more below.

Apart from the bottom side erosion pattern and stagnation effect, both material derivative formulated erosion indicators $(DP/Dt)/V_{cell}$ and $(DP/Dt)^2$ in MAX1 predict well the erosion pattern on the top side of the orifice. For all indicators in MAX2, there is a clear erosion pattern on the top side of the orifice that agrees well with experiments.

4.3.3. TS model — RANS

The visualizations provided in Fig. 19 present the potential erosion areas within the injector orifice for the TS model using the MAX1 and MAX2 algorithms. These results can easily be compared with the CAD model — RANS results (Fig. 17) to understand the effect of surface deviations on the erosion assessment results.

For MAX1 (Figs. 19(a)–19(d)), a stagnation effect is still present and affecting almost all erosion indicators, but in this case high values are more persistent on the top side of the orifice for material derivative indicators ($(DP/Dt)/V_{cell}$, $(DP/Dt)^2$).

Hence, the erosion pattern is located on the top side of the orifice, similarly as in CAD model result, but the extent of the erosion pattern is much longer than the CAD model — RANS results. For MAX2 (Figs. 19(e)–19(h)), there is a good agreement with experiments for almost all erosion indicators. Hence, it can be concluded that the overall agreement with experiment is much better with the presence of surface deviations with RANS.

4.3.4. TS model — LES

In the MAX1 algorithm results (Figs. 20(a)–20(d)), all erosion indicators show higher values on the top side of the orifice than on the bottom side. Excluding the aforementioned stagnation effect, there is a good agreement with high lift experiments. This also agrees well with previous conclusions from a force history comparison (Fig. 15(d)) and the collapse mechanism illustrations (Fig. 16).

In contrast, the MAX2 algorithm (Figs. 20(e)–20(h)) displays damage on the bottom side, as seen in the CAD model — LES results (Figs. 18(e)–18(f)), and it is more dispersed across the entire orifice surface. The extent of the damage, indicated by the red-colored areas, is slightly greater on the top surface but not to the extent shown by the MAX1 algorithm. A direct comparison of the $(DP/Dt)^2$ erosion indicator between both algorithms (Figs. 20(c)–20(g)) highlights these differences.

In Fig. 21, orifice wall surfaces for the erosion assessment are offset (towards internal domain) with a distance of 10 μm. In this way, the effect of the surface deviations is considered to be limited. Here, the top side damage is dramatically higher than the bottom side. Comparing these results with those where no offset was applied (as shown in Fig. 20(e)) reveals a substantial difference in the patterns and extent of erosion damage.

Therefore, these findings suggest that the LES simulation of the TS model using the MAX2 algorithm is highly sensitive to surface deviations. This sensitivity arises because the LES resolves a wider range of turbulent scales and it allows for a better prediction of the local pressure fluctuations, thereby capturing the finer details of the flow field and turbulence structures that significantly influence the mass transfer rate. Hence, the enhanced mass transfer rate condition (Condition3 in the MAX2 algorithm in Fig. 1) makes the MAX2 algorithm vulnerable to those surface deviations and manipulates the overall erosion pattern.

4.3.5. TS model 8-hole — RANS

Fig. 22 present the erosion assessment results in both MAX1 and MAX2 algorithms from top and bottom view. Here, the results are presented only with the $(DP/Dt)^2$ erosion indicator, which was the most reliable for both algorithms in the TS model 1-hole — RANS results (see Fig. 19) erosion assessment. Overall, the results are in good agreement with experiments. Maximum values take place on the top side of each hole. Similarly as in previous results, MAX2 prevents fake collapses, and this eliminates the bottom side erosion patterns that weakly exist in the MAX1 algorithm. This consistency with Brunhart [21] highlights the reliability of $(DP/Dt)^2$ erosion indicator. Numerical results further support that having identical surface deviations for each hole creates distinct erosion patterns. This makes the overall erosion assessment much more complicated.

As previously mentioned in the methodology section, hole7 was selected for TS model 1-hole simulations among the other injector holes. In Fig. 22, this hole is specially marked. A direct comparison between these results and the TS model 1-hole — RANS results (see Fig. 19) states that asymmetric top side erosion pattern is consistently apparent despite different mesh resolutions.

5. Conclusion

This study explores the numerical assessment of cavitation-induced erosion in high-pressure fuel injectors using computational fluid dynamics (CFD), emphasizing the role of surface deviations and the trade-offs between Reynolds-Averaged Navier–Stokes (RANS) and Large Eddy Simulation (LES) methodologies. Cavitation is modeled using the mixture transport with the modified Zwart–Gerber–Belamri approach. The numerical results are compared with the experimental erosion data. To examine the effect of the surface deviations to erosion patterns, high lift condition is modeled with Computer Aided Design (CAD) and Tomography Scan (TS) models separately.

The key findings and contributions are summarized as follows:

- Compared to idealized CAD geometries, TS models reduce vapor volumes and alter erosion distributions, providing a more realistic representation of experimental conditions. This demonstrates the importance of incorporating realistic geometrical deviations into erosion assessments.
- The MAX2 algorithm prevents fake collapses and provides precise, localized erosion predictions.
- Among four evaluated indicators (P, $(DP/Dt)/V_{\text{cell}}$, $(DP/Dt)^2$, and PPD2), $(DP/Dt)^2$ emerged as the most reliable for identifying erosion-prone regions. The proposed erosion framework aligns well with experimental observations, enhancing the predictive accuracy of cavitation erosion modeling.
- LES captures more detailed cavitation structures and turbulence interactions, offering higher fidelity in physics. RANS, on the other hand, is capable of providing general flow features.
- LES simulations with the TS model are particularly sensitive to surface deviations due to their ability to resolve finer turbulence scales, which capture detailed flow and pressure fluctuations influencing erosion. Hence, special attention must be paid if LES is to be used in the presence of surface deviations.

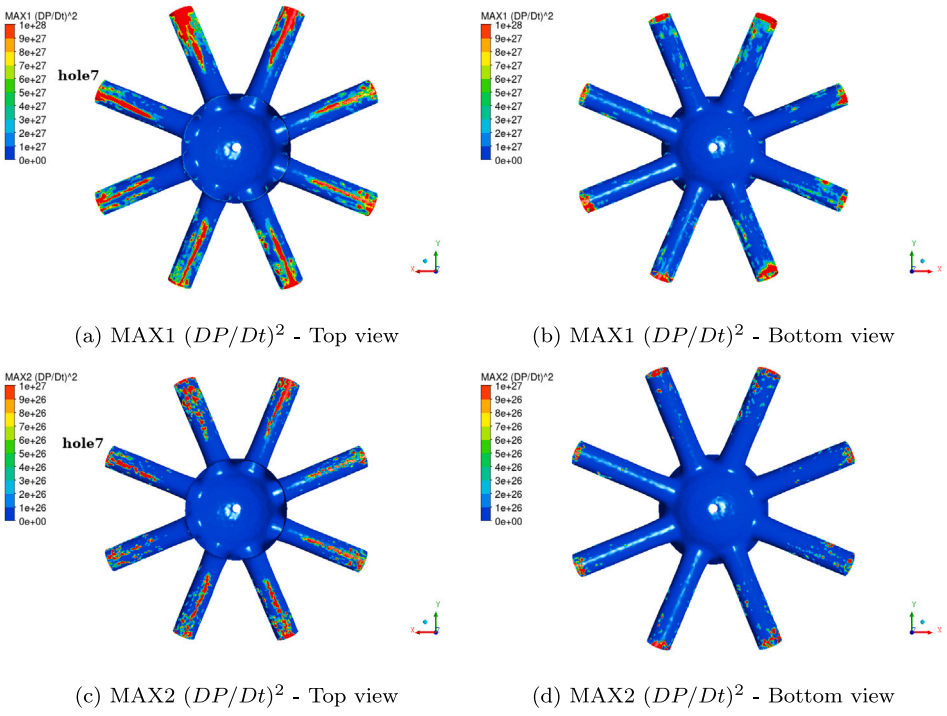

(a) MAX1 $(DP/Dt)^2$ - Top view (b) MAX1 $(DP/Dt)^2$ - Bottom view

(c) MAX2 $(DP/Dt)^2$ - Top view (d) MAX2 $(DP/Dt)^2$ - Bottom view

Fig. 22. Erosion assessment with MAX1 and MAX2 $(DP/Dt)^2$ – TS model 8-hole – RANS.

- RANS simulations with the TS model provide good accuracy at significantly lower computational cost (LES is roughly 32 times more expensive than RANS), making them suitable for early-stage design assessments.

By bridging the gap between academic models and industrial applications, this study provides valuable insights for designing more durable and efficient high-pressure fuel injectors. The integration of realistic surface deviations into numerical models establishes a new standard for erosion risk assessments in fuel injection systems. Together with the findings, the proposed approach is also applicable to a broad range of cavitation-prone systems, such as hydraulic components and marine propellers, enabling more accurate and reliable erosion predictions.

Future work will investigate the following topics in detail;

- Investigate the effect of surface deviations under low-lift needle conditions.
- Perform LES simulations for 8-hole injectors in both low and high-lift scenarios.
- Investigate the impact of transient needle dynamics, including start-up and needle closure phases, which are critical for accurately capturing erosion-sensitive regions.

CRediT authorship contribution statement

Mehmet Özgünoğlu: Writing – original draft, Visualization, Validation, Software, Methodology, Investigation, Conceptualization. **Gerard Mouokue:** Writing – review & editing, Resources. **Michael Oevermann:** Writing – review & editing, Supervision. **Rickard E. Bensow:** Writing – review & editing, Supervision, Funding acquisition.

Declaration of competing interest

The authors declare that they have no known competing financial interests or personal relationships that could have appeared to influence the work reported in this paper.

Acknowledgments

This project is funded by the European Union Horizon 2020, the EDEM project, a Marie Skłodowska-Curie Action Innovative Training Network project, grant number 861002. The simulations were performed on the resources provided by the National Academic Infrastructure for Supercomputing in Sweden (NAISS) and the Swedish National Infrastructure for Computing (SNIC) at Chalmers Centre for Computational Science and Engineering (C3SE) and National Supercomputer Center at Linköping University (NSC).

References

[1] MEPC, Resolution. 2023 IMO strategy on reduction of GHG emissions from ships. 2023.
[2] Nouri JM, Mitroglou N, Yan Y, Arcoumanis C. Internal flow and cavitation in a multi-hole injector for gasoline direct-injection engines. In: SAE world congress and exhibition. SAE International; 2007, http://dx.doi.org/10.4271/2007-01-1405.
[3] Prasetya R, Sou A, Oki J, Nakashima A, Nishida K, Wada Y, Ueki Y, Yokohata H. Three-dimensional flow structure and string cavitation in a fuel injector and their effects on discharged liquid jet. Int J Engine Res 2021;22(1):243–56. http://dx.doi.org/10.1177/1468087419835697.
[4] Schmidt SJ, Mihatsch MS, Thalhamer M, Adams NA. Assessment of Erosion Sensitive Areas via compressible simulation of unsteady cavitating flows. In: Kim K-H, Chahine G, Franc J-P, Karimi A, editors. Fluid Mech Appl 2014;329–44. http://dx.doi.org/10.1007/978-94-017-8539-6_14.
[5] Dular M, Stoffel B, Širok B. Development of a cavitation erosion model. Wear 2006;261(5):642–55. http://dx.doi.org/10.1016/j.wear.2006.01.020.
[6] Dular M, Coutier-Delgosha O. Numerical modelling of cavitation erosion. Internat J Numer Methods Fluids 2009;61(12):1388–410. http://dx.doi.org/10.1002/fld.2003.
[7] Bensow RE, Bark G. Implicit LES predictions of the cavitating flow on a propeller. J Fluids Eng 2010;132(4):041302. http://dx.doi.org/10.1115/1.4001342.
[8] Li Z-r, Pourquie M, van Terwisga T. Assessment of cavitation erosion with a URANS method. J Fluids Eng 2014;136(4):041101. http://dx.doi.org/10.1115/1.4026195.
[9] Mihatsch MS, Schmidt SJ, Adams NA. Cavitation erosion prediction based on analysis of flow dynamics and impact load spectra. Phys Fluids 2015;27(10):103302. http://dx.doi.org/10.1063/1.4932175.
[10] Peters A, Sagar H, Lantermann U, el Moctar O. Numerical modelling and prediction of cavitation erosion. Wear 2015;338–339:189–201. http://dx.doi.org/10.1016/j.wear.2015.06.009.

[11] Peters A, el Moctar O. Numerical assessment of cavitation-induced erosion using a multi-scale Euler–Lagrange method. J Fluid Mech 2020;894:A19. http://dx.doi.org/10.1017/jfm.2020.273.
[12] Schenke S, van Terwisga TJ. An energy conservative method to predict the erosive aggressiveness of collapsing cavitating structures and cavitating flows from numerical simulations. Int J Multiph Flow 2019;111:200–18. http://dx.doi.org/10.1016/j.ijmultiphaseflow.2018.11.016.
[13] Arabnejad MH, Svennberg U, Bensow RE. Numerical assessment of cavitation erosion risk using incompressible simulation of cavitating flows. Wear 2021;464–465:203529. http://dx.doi.org/10.1016/j.wear.2020.203529.
[14] Arabnejad MH, Svennberg U, Bensow RE. Numerical assessment of cavitation erosion risk in a commercial water-jet pump. J Fluids Eng 2022;144(5):051201. http://dx.doi.org/10.1115/1.4052634.
[15] Örley F, Hickel S, Schmidt SJ, Adams NA. Large-eddy simulation of turbulent, cavitating fuel flow inside a 9-hole diesel injector including needle movement. Int J Engine Res 2017;18(3):195–211. http://dx.doi.org/10.1177/1468087416643901.
[16] Kolovos K, Kyriazis N, Koukouvinis P, Vidal A, Gavaises M, McDavid RM. Simulation of transient effects in a fuel injector nozzle using real-fluid thermodynamic closure. Appl Energy Combust Sci 2021;7:100037. http://dx.doi.org/10.1016/j.jaecs.2021.100037.
[17] Falsafi S, Blume M, Klaua T, Indrich M, Wloka J, Skoda R. Numerical simulation of cavitating flow in maritime high-pressure direct fuel injection nozzles and assessment of cavitation-erosion damage. Int J Engine Res 2023;24(2):393–407. http://dx.doi.org/10.1177/14680874211052138.
[18] Gomez Santos E, Shi J, Venkatasubramanian R, Hoffmann G, Gavaises M, Bauer W. Modelling and prediction of cavitation erosion in GDi injectors operated with E100 fuel. Fuel 2021;289:119923. http://dx.doi.org/10.1016/j.fuel.2020.119923.
[19] Koukouvinis P, Gavaises M, Li J, Wang L. Large eddy simulation of diesel injector including cavitation effects and correlation to erosion damage. Fuel 2016;175:26–39. http://dx.doi.org/10.1016/j.fuel.2016.02.037.
[20] Koukouvinis P, Karathanassis IK, Gavaises M. Prediction of cavitation and induced erosion inside a high-pressure fuel pump. Int J Engine Res 2018;19(3):360–73. http://dx.doi.org/10.1177/1468087417708137.
[21] Brunhart M. Cavitation and the application of methods for erosion prediction in high pressure fuel injection systems [Ph.D. thesis], City, University of London; 2020, URL https://openaccess.city.ac.uk/id/eprint/24723/.
[22] Fortes Patella R, Archer A, Flageul C. Numerical and experimental investigations on cavitation erosion. IOP Conf Series: Earth Environ Sci 2012;15:2013. http://dx.doi.org/10.1088/1755-1315/15/2/022013.
[23] Cristofaro M, Edelbauer W, Koukouvinis P, Gavaises M. Large eddy simulation of the internal injector flow during pilot injection. In: Proceedings of the 10th international symposium on cavitation. ASME Press; 2018, http://dx.doi.org/10.1115/1.861851_ch127.
[24] Cristofaro M, Edelbauer W, Koukouvinis P, Gavaises M. A numerical study on the effect of cavitation erosion in a diesel injector. Appl Math Model 2020;78:200–16. http://dx.doi.org/10.1016/j.apm.2019.09.002.
[25] Cristofaro M, Edelbauer W, Koukouvinis P, Gavaises M. Influence of diesel fuel viscosity on cavitating throttle flow simulations under erosive operation conditions. ACS Omega 2020;5(13):7182–92. http://dx.doi.org/10.1021/acsomega.9b03623, PMID: 32280858.
[26] Morozov AV, Iben U, Bosch R. Experimental analysis and simulation of cavitating throttle flow. 2008.
[27] Zhang L, He Z, Guan W, Wang Q, Som S. Simulations on the cavitating flow and corresponding risk of erosion in diesel injector nozzles with double array holes. Int J Heat Mass Transfer 2018;124:900–11. http://dx.doi.org/10.1016/j.ijheatmasstransfer.2018.03.086.
[28] Kumar A, Ghobadian A, Nouri J. Numerical simulation and experimental validation of cavitating flow in a multi-hole diesel fuel injector. Int J Engine Res 2022;23(6):958–73. http://dx.doi.org/10.1177/1468087421998631.
[29] Wang C, Adams M, Luo T, Jin T, Luo F, Gavaises M. Hole-to-hole variations in coupled flow and spray simulation of a double-layer multi-holes diesel nozzle. Int J Engine Res 2021;22(10):3233–46. http://dx.doi.org/10.1177/1468087420963986.
[30] Magnotti GM, Battistoni M, Saha K, Som S. Development and validation of the cavitation-induced erosion risk assessment tool. Transp Eng 2020;2:100034. http://dx.doi.org/10.1016/j.treng.2020.100034.
[31] Mariasiu F. Numerical investigation of the effects of biofuel characteristics on the injector nozzle erosion process. Tribol Trans 2013;56(2):161–8. http://dx.doi.org/10.1080/10402004.2012.709918.
[32] Mouvanal S, Chatterjee D, Bakshi S, Burkhardt A, Mohr V. Numerical prediction of potential cavitation erosion in fuel injectors. Int J Multiph Flow 2018;104:113–24. http://dx.doi.org/10.1016/j.ijmultiphaseflow.2018.03.005.
[33] Lu P, Xu Z, Tian Y, Yang R, Hu K, Li H, et al. Effect of initial surface scratches on the cavitation erosion behavior of 316l stainless steel substrates and 316l stainless steel coatings. Materials 2023;16(4). http://dx.doi.org/10.3390/ma16041392.
[34] Lin J, Wang Z, Cheng J, Kang M, Fu X, Hong S. Effect of initial surface roughness on cavitation erosion resistance of arc-sprayed fe-based amorphous/nanocrystalline coatings. Coatings 2017;7(11). http://dx.doi.org/10.3390/coatings7110200.
[35] Menter FR. Zonal two equation k-w turbulence models for aerodynamic flows. 1993, URL https://api.semanticscholar.org/CorpusID:130535195.
[36] Nicoud F, Ducros F. Subgrid-scale stress modelling based on the square of the velocity gradient tensor. Flow Turbul Combust 1999;62(3):183–200.
[37] Reboud JL, Stutz B, Coutier O. Two-phase flow structure of cavitation : Experiment and modelling of unsteady effects. 1998, URL https://api.semanticscholar.org/CorpusID:107617247.
[38] Zwart PJ, Gerber AG, Belamri T, et al. A two-phase flow model for predicting cavitation dynamics. In: Fifth international conference on multiphase flow, vol. 152. Yokohama Japan; 2004.
[39] ANSYS, Inc. ANSYS fluent theory guide. 2021, Canonsburg, Pennsylvania, USA. 2021 R1 edition.
[40] Budich B, Schmidt SJ, Adams NA. Numerical simulation and analysis of condensation shocks in cavitating flow. J Fluid Mech 2018;838:759–813. http://dx.doi.org/10.1017/jfm.2017.882.
[41] Koukouvinis P, Naseri H, Gavaises M. Performance of turbulence and cavitation models in prediction of incipient and developed cavitation. Int J Engine Res 2017;18(4):333–50. http://dx.doi.org/10.1177/1468087416658604.
[42] Coutier-Delgosha O, Fortes-Patella R, Reboud JL. Simulation of unsteady cavitation with a two-equation turbulence model including compressibility effects. J Turbul 2002;3:N58. http://dx.doi.org/10.1088/1468-5248/3/1/058.
[43] Mihatsch MS, Schmidt SJ, Thalhamer M, Adams NA. Numerical prediction of erosive collapse events in unsteady compressible cavitating flows. In: MARINE 2011, IV international conference on computational methods in marine engineering: selected papers. Dordrecht: Springer Netherlands; 2013, p. 187–98. http://dx.doi.org/10.1007/978-94-007-6143-8_11.
[44] GOM GmbH. GOM Inspect. Version 2022.
[45] Davidson L. Large eddy simulations: How to evaluate resolution. Int J Heat Fluid Flow 2009;30(5):1016–25. http://dx.doi.org/10.1016/j.ijheatfluidflow.2009.06.006, The 3rd International Conference on Heat Transfer and Fluid Flow in Microscale.
[46] Pope SB. Turbulent flows. Cambridge University Press; 2000.
[47] Celik IB, Cehreli ZN, Yavuz I. Index of resolution quality for large eddy simulations. J Fluids Eng 2005;127(5):949–58. http://dx.doi.org/10.1115/1.1990201.
[48] Befrui B, Corbinelli G, Robart D, Reckers W, Weller H. LES simulation of the internal flow and near-field spray structure of an outward-opening GDi injector and comparison with imaging data. In: SAE world congress and exhibition. SAE International; 2008, http://dx.doi.org/10.4271/2008-01-0137.
[49] Jeong J, Hussain F. On the identification of a vortex. J Fluid Mech 1995;285:69–94. http://dx.doi.org/10.1017/S0022112095000462.
[50] Salvador F, Martínez-López J, Romero J-V, Roselló M-D. Computational study of the cavitation phenomenon and its interaction with the turbulence developed in diesel injector nozzles by large eddy simulation. Math Comput Modelling 2013;57(7):1656–62. http://dx.doi.org/10.1016/j.mcm.2011.10.050.
[51] Masuda R, Fuyuto T, Nagaoka M, von Berg E, Tatschl R. Validation of diesel fuel spray and mixture formation from nozzle internal flow calculation. In: 2005 SAE Brasil fuels and lubricants meeting. SAE International; 2005, http://dx.doi.org/10.4271/2005-01-2098.